Micro-distribution of Oxygen Isotopes in Unequilibrated Enstatite Chondrites

Michael K. Weisberg[1,2,3], Noriko T. Kita[4], Kohei Fukuda[4], Guillaume Siron[4] and Denton S. Ebel[2,3]

[1]Dept. Physical Sci., Kingsborough College CUNY, Brooklyn, NY 11235.

(mweisberg@kbcc.cuny.edu)

[2]Dept. Earth and Environmental Sci., CUNY Graduate Center, New York, NY 10016.

[3]Dept. Earth and Planetary Sci., American Museum of Natural History, New York, NY 10024.

[4]WiscSIMS, Dept. of Geoscience, University of Wisconsin-Madison, Madison, WI 53706.

Submitted to Geochimica et Cosmochimica Acta

Revised and resubmitted 2/5/2021

Abstract

We report petrology and high precision, *in situ* oxygen isotope analyses of silicates in chondrules, fragments, metal-rich nodules, refractory inclusions from the ALH 81189 (EH3), ALH 85159 (paired with ALH 81189) and from the MAC 88136 (EL3) chondrite. This is the first report of oxygen isotope ratios for individual objects in an EL3 and for the silicates associated with the metal-rich nodules that are characteristic of unequilibrated enstatite (E3) chondrites. The oxygen isotopic data from the chondrules and other objects form a trend, on a 3-isotope plot, that coincides with the slope~1 primitive chondrule mineral (PCM) line (initially defined by chondrules from the Acfer 094 primitive carbonaceous chondrite), with most objects clustering at the intersection of the PCM line with the terrestrial fractionation (TF) line, near whole rock E3. The data from EH3 and EL3 overlap and show a similar distribution, suggesting they formed from a similar pool of precursors or in similar gaseous environments, but their mineral compositions suggest differences in their nebular environments and/or parent bodies. Silicates in the metal-rich nodules we analyzed (in both EH3 and EL3) have oxygen isotope ratios (as well as mineral compositions) similar to the silicate (metal-free) chondrules. This is consistent with formation of the metal-rich nodules prior to chondrite accretion, in an environment and from a process similar to that which formed the coexisting chondrules, but from more metal-rich mixtures of precursors. Olivine in an AOA from ALH 81189 is ^{16}O-rich with $\delta^{18}O = -46.5‰$, $\delta^{17}O = -48.0‰$, similar to the AOAs and refractory inclusions previously reported in E3 and in all other chondrite groups. There is a clear distinction in oxygen isotopic compositions between the chondrules in the E3 chondrites and those in the LL and R as well as those in CV and CM chondrite groups. Chondrules from CR and E chondrites plot closer to the PCM line than all other chondrite groups with E3 chondrules having a different distribution toward more ^{16}O-poor compositions. Chondrules in other chondrite groups form trends

above and below the PCM. From the distribution of EC chondrules along the PCM line, we propose that similar pools of chondrule precursors were present in the different (carbonaceous, CR and Acfer 094 and non-carbonaceous, E) chondrule forming regions in the protoplanetary disk but with different amounts of ^{16}O-rich refractory materials, prior to development of the postulated *Jupiter divide* that potentially separated inner (non-carbonaceous) from outer (carbonaceous chondrite) Solar System materials or the Jupiter barrier was inefficient in completely separating these materials.

Introduction

Enstatite chondrites are important for constraining conditions and processes in the protoplanetary disk and they may be our closest examples of the material that accreted to form the terrestrial planets (e.g., Javoy 1995, 2010; Dauphas, 2017). They are among the most reduced solar system materials as indicated by their unique mineral assemblages and compositions (e.g., Keil, 1968; Weisberg and Kimura, 2012). Their whole rock stable (O, Cr, Ti, Ni and Zn) isotopic compositions are markedly similar to those of the Earth-Moon system (Javoy, 1995; Warren, 2011; Paniello, 2012), but Si isotopes differ, possibly supplying evidence against a direct relationship between E chondrites and the Earth -Moon system (Fitoussi and Bourdon, 2012; Savage and Moynier, 2013; Kadlag et al., 2019). However, metal-silicate Si isotope fractionation in a reduced nebular environment and vapor loss of lighter Si isotopes during planetary volatilization may have contributed to differences in the Si isotopic compositions between Earth and the E chondrites (Sikdar and Rai, 2020). It was recently shown that H, C and N isotopic compositions of E chondrites are also similar to Earth (Piani et al., 2020; Gray et al., 2021) and that enstatite chondrites contain enough H to have delivered to Earth three times the amount of water currently in its oceans. (Piani et al., 2020). The surface chemistry of Mercury suggests reduced E chondrite-like precursors (e.g., Nittler et al., 2011; Burbine et al., 2002; Ebel and Stewart, 2018). Thus, the E chondrites may be similar to the materials that were present in specific feeding zones during accretion of the terrestrial planets.

We previously studied the petrology and oxygen isotopic compositions of chondrules in the Sahara 97096, Yamato 691, Kota Kota and LEW 87223 E3 chondrites and showed that they define a slope~1 line, termed the enstatite chondrite mixing (ECM) line (Weisberg et al., 2010, 2011),

which is indistinguishable from the primitive chondrule mineral (PCM) line defined by Acfer 094 chondrules (Ushikubo et al., 2012). Here we report new, high precision, *in situ* oxygen isotopic analyses of 31 objects (chondrules, refractory inclusions and metal-rich nodules) in the highly primitive Allan Hills (ALH) 81189 (and paired ALH 85159) EH3 and, to our knowledge, the first oxygen isotopic analyses of individual objects in an EL3 chondrite, MacAlpine Hills (MAC) 88136. The goals of this work are to study the micro-distributions of oxygen isotopic compositions in chondrules and other objects in the most primitive EH3 and EL3 chondrites, further test the relationship between enstatite chondrite precursors and the precursors of other primitive chondrites (e,g., Acfer 094), explore the relationship between silicates among the different types of objects (including the reduced chondrules, metal-rich nodules, FeO-rich silicates and refractory inclusions) and better document and develop an understanding of the oxygen isotopic differences among the chondrules in primitive chondrites.

Background

The distribution of three stable oxygen isotopes in chondrules at the micron scale has provided important insights into the process of isotope exchange between chondrule melt and surrounding gas (e.g., Yu et al., 1995; Boesenberg et al., 2005). *In situ* oxygen isotopic secondary ion mass spectroscopy (SIMS) analyses of chondrules in carbonaceous chondrites has revealed the existence of ^{16}O-rich relict olivine grains (e.g., Yurimoto and Wasson, 2002; Jones et al., 2004; Kunihiro et al., 2004; Rudraswami et al. 2011; Ushikubo et al. 2012; Tenner et al. 2013; Marrocchi et al. 2018; 2019). However, excluding the minor occurrence of relict grains, minerals and glass in individual chondrules show indistinguishable oxygen isotope ratios (e.g., Ushikubo et al. 2013; Tenner et al. 2015), in contrast to earlier observations by Chaussidon et al. (2008) that reported pyroxene and

mesostasis being ^{16}O-depleted in oxygen isotope ratios compared to olivine within the same chondrules. Reaction of chondrules with SiO molecules during chondrule formation has also been proposed to explain petrologic features, such as mineralogical zoning in chondrules (pyroxene-rich shells) (e.g., Tissandier et al., 2002; Libourel et al., 2006), which are likely the result of chondrules forming in open systems with respect to major oxides (Nagahara et al., 2008; Libourel and Portail, 2018). Under open-system chondrule formation, oxygen isotope exchange would have occurred efficiently between chondrule melt and the ambient gas (containing SiO, H_2O, and CO molecules) and resulted in internally homogeneous oxygen isotope ratios in each chondrule (Kita et al., 2010; Ushikubo et al., 2012; Tenner et al., 2015; Marrocchi and Chaussidon, 2015). Tenner et al. (2015) presented a mass balance model involving ^{16}O-poor water ice and solid precursors to explain their observation of systematic changes in $\Delta^{17}O$ ($=\delta^{17}O–0.52\times \delta^{18}O$) with redox state of the chondrules in CR chondrites, which was further applied to chondrules in CV (Hertwig et al. 2018). Marrocchi and Chaussidon (2015) presented a model in which SiO molecules played a major roles in controlling mass independent fractionation of oxygen isotopes among chondrules in carbonaceous chondrites. In the case of ordinary chondrite chondrules, Kita et al. (2010) suggested that the chondrule-forming region contained two kinds of solid precursors, (1) ^{16}O-poor solid precursors and (2) ^{16}O-rich solid precursors derived from the same oxygen isotope reservoir as carbonaceous chondrites. These two sources were mixed efficiently among chondrules as a result of open system behavior during chondrule formation through interactions between the heated chondrules and the ambient gas.

For the enstatite chondrites, Clayton and Mayeda (1985) indicated that individual chondrules from EH3 chondrites form a distinct cluster on the oxygen 3-isotope diagram, not overlapping chondrules from O or C chondrites and scattering about a best-fit line of slope 0.7. In contrast,

Tanaka and Nakamura (2017) reported the best-fit line with the slope of 1.27 from chondrules in EH3 and EH4 chondrites that include data from 6 individual chondrules in EH3. However, our previous results on chondrules in four E3 chondrites showed that the oxygen isotope ratios ($\delta^{18}O$, $\delta^{17}O$) of olivine and pyroxene in E3 chondrules have a wide range of values spanning as much as 10 ‰ in both $\delta^{18}O$ and $\delta^{17}O$. Some chondrules from EH3 chondrites cluster around the terrestrial fractionation line near enstatite chondrite whole rock values, some chondrules overlap the ordinary chondrite field on the 3-isotope diagram and some extend toward more ^{16}O-rich compositions similar to C chondrite chondrules (Weisberg et al., 2011). Olivine in some E3 chondrules shows a wide range of $\Delta^{17}O$ values (−4‰ to +2‰) that form a mixing line parallel to but distinct from the carbonaceous chondrite anhydrous mixing (CCAM) line (e.g., Clayton and Mayeda, 1984). This E3 chondrule olivine line was defined as the enstatite chondrite mixing (ECM) line (Weisberg et al., 2011) but, as mentioned above, it coincides with the line defined by chondrules from Acfer 094 referred to as the PCM (primitive chondrite mineral) line by Ushikubo et al. (2012).

Another important issue regarding the E chondrites is the origin of the more oxidized components in E3 chondrites. FeO-bearing silicates in enstatite chondrites are relatively rare and apparently out of equilibrium with the more typical reduced (e.g., near-pure enstatite) mineral compositions (e.g., Lusby et al. 1987; Weisberg et al., 1994). Weisberg et al. (1994) showed that the FeO-bearing silicates are older than the FeO-poor silicates, marking a more oxidized pre-history for these meteorites. It has been suggested that these minerals were transported from ordinary chondrite source regions to the E chondrite accretion zones (Lin et al., 2002). However, the FeO-bearing pyroxene in E3 chondrites has oxygen isotope values similar to coexisting pure enstatite, suggesting it formed locally and was not transported from the ordinary or other chondrule-forming region (Kimura et al., 2003; Weisberg et al., 2011). Additionally, the petrologic setting of the FeO-

bearing pyroxene (enclosed in enstatite) suggests that it predates the reduced, FeO-poor enstatite-rich mineral assemblages and implies that conditions were initially more oxidizing in the E3 chondrule-forming region and/or that the mixture of chondrule precursors for E chondrites was, at least in part, compositionally similar to chondrule precursors of other chondrite groups. This is supported by the oxidation states of Ti in silicates, which contain a mixture of Ti^{3+} and Ti^{4+} (Simon et al., 2016).

Weisberg et al. (2011) reported oxygen isotopic heterogeneity among mineral grains within some of the chondrules in E3 chondrites. They suggested that this implies incomplete melting of the chondrules, survival of minerals from previous generations of chondrules, and chondrule recycling or possibly open system behavior during chondrule formation. One chondrule contained a relict grain with an R chondrite-like oxygen isotopic composition. The presence of R chondrite-like oxygen in a large, possibly relict, olivine grain suggests limited mixing of materials from other reservoirs and/or close proximity of E, O and R chondrite precursors.

Interestingly, the relatively rare calcium-aluminum-rich inclusions (CAIs) in E3 chondrites have petrologic characteristics and ^{16}O-rich oxygen isotopic compositions similar to CAIs in other chondrite groups and appear to have formed in a different oxygen reservoir from the E3 chondrules (Guan et al., 2000; Fagan et al., 2001; Lin et al., 2003). This suggests that CAIs in all chondrite groups may all have formed in the same region and then been distributed to the accretion zones of the various chondrite groups. However, oxygen isotopes indicate that formation and distribution of chondrules and their precursors was more complicated, with chondrules from each chondrite group forming in their own separate regions, from distinct reservoirs, presumably representing different heliocentric distances or nebular epochs.

Methods

We selected 22 objects (chondrules, fragments, metal nodules, refractory inclusions) from thin section ALH 81189, 3 (EH3), 9 objects from ALH 85159, 5 (paired with ALH 81189) and 13 objects from MAC 88136, 37 (EL3) for oxygen isotope analysis. Element maps for all sections, back-scattered electron (BSE) images of each object and major mineral compositions were collected using a combination of electron beam instruments.

Wavelength dispersive spectroscopic (WDS) maps of Si, Al, Mg, Ca, Fe, Ti, S, P, Na and Ni X-ray emission intensity of each thin section were generated with a Cameca SX100 electron microprobe (at the AMNH). These are "stage maps" (moving stage, stationary electron beam). Operating conditions were 15 kV accelerating voltage and 40 nA beam current, with a dwell time of 12 ms on one micrometer beam spots spaced 4 to 7 microns apart. Modal analysis was based on these elemental X-ray maps. Mineral compositions were determined on nominally 1 μm spots using the Cameca SX100 and JEOL Super Probe (at Rutgers) electron microprobes. Natural and synthetic standards were chosen based on the compositions of the minerals being analyzed. An accelerating potential of 15 keV and a sample current of 20 nA were used for silicates and 20 keV and 25 nA for metal. Counting times were 20 s on peak, and 10 s on background (off-peak) spectrometer positions. Relative uncertainties (2 sigma) based on counting statistics for major elements (Si, Fe, Mg) are calculated to be <2% and for Ti, Cr, Mn and Ca they are 10%, 10%, 9% and 5%, respectively. Data reductions were carried out using instrument software based on methods described by Pouchou and Pichoir (1991).

Oxygen isotopes of silicates were analyzed *in situ*, using the Cameca IMS 1280 secondary ion mass spectrometer at the WiscSIMS laboratory. The goal was to measure six grains (olivine and pyroxene) in each object, if grain size allowed, to achieve a representative average and to test for internal homogeneity within each chondrule or other object. The analytical procedure was similar

188 to that described in Kita et al. (2010). A Cs^+ primary ion beam was focused to 12 μm diameter at
189 2 nA. Secondary oxygen ions ($^{16}O^-$, $^{17}O^-$, and $^{18}O^-$) were detected simultaneously using multi-
190 collector Faraday cups with three feedback resistors, 10^{10} ohm, 10^{12} ohm, and 10^{11} ohm for $^{16}O^-$,
191 $^{17}O^-$, and $^{18}O^-$, respectively. As in previous studies, 16-25 unknown analyses were bracketed by 8
192 analyses of a San Carlos olivine reference material (SC-Ol; $\delta^{18}O = 5.32‰$; Kita et al., 2010). Two
193 additional olivine, three pyroxene, and one quartz reference materials were also analyzed to correct
194 instrumental bias (appendix). Average external reproducibility of bracketed SC-Ol analyses (2SD)
195 was ~0.2 ‰ for $\delta^{18}O$ and 0.3 ‰ for $\delta^{17}O$ and $\Delta^{17}O$. The external reproducibilities (2SD) for each
196 bracket are assigned as the uncertainties of bracket unknown analyses.
197
198 **Results**
199 *Petrology*
200 The objects we studied from ALH 81189 (Fig. 1a) and paired ALH 85159 (Fig. 1b) included
201 20 porphyritic pyroxene (PP), 1 PP with FeO-rich pyroxene, 2 porphyritic olivine-pyroxene (POP),
202 2 porphyritic olivine (PO), and 1 barred pyroxene chondrule; 1 amoeboid olivine aggregate
203 (AOA); 1 diopside-plagioclase fragment; 2 isolated olivine fragments; and 1 metal-rich nodule
204 containing enstatite (En_{98}). From MAC 88136 (Fig. 1c) we studied an unusually large (>1mm)
205 diopside-rich chondrule, a silica-pyroxene chondrule, a radial pyroxene (RP) and 7 PP chondrules,
206 and 3 metal-rich nodules containing enstatite laths. The latter are the first oxygen isotopic data
207 from silicates in metal-rich nodules in E3 chondrites.
208 As is typical of EH3 and EL3, most chondrules are dominantly FeO-poor enstatite and can be
209 considered type IB (Figs. 2a-d). All textural types of Gooding and Keil (1968) are present in
210 enstatite chondrites but (type I) porphyritic pyroxene (PP, e.g., Fig. 2b) is the most common type.

Most of the PP chondrules we studied contain near-endmember enstatite ($En_{>98}$). One PP (C9) in ALH 81189 was dominated by FeO-rich pyroxene ($Wo_{0.1}En_{73-83}$) (Fig. 2c). Unlike most other chondrite groups, olivine is minor in the E3 chondrites. It occurs mainly as poikilitically enclosed grains in enstatite in the pyroxene-rich chondrules, but we also identified rare porphyritic olivine (PO) chondrules and relatively large, isolated olivine mineral fragments (Fo_{98}) up to 300 μm in size in ALH 81189 (Fig. 2a).

Several unusual objects were also studied including a diopside–plagioclase chondrule (F9) in ALH 81189 unlike any chondrule or fragment previously described in any E3 chondrite. It is irregular in shape, ~300 μm across and composed mainly of laths of diopside ($Wo_{44.8}En_{54.3}$) having 2.5 wt.% Al_2O_3 and 1.5 TiO_2 and plagioclase ($An_{79.5}Ab_{20.5}$), with minor enstatite ($Wo_{0.6}En_{97.1}$) and silica (Fig. 3a). The AOA (F17) in ALH 81189 is an irregularly shaped inclusion consisting of olivine surrounding nodules of Ca-pyroxene and anorthite (Fig. 3b) and is texturally and mineral compositionally similar to AOAs in C chondrites (e.g., Grossman and Steele, 1976). The olivine has a composition of Fo_{99}, if calculated based on two end members (Fo and Fa). However, this olivine also contains 0.3 wt. % CaO.

The diopside-rich chondrule (C1) in MAC 88136 is ~50% coarse diopside ($Wo_{46.4}\ En_{53.2}$) in thin section, occurring with enstatite ($Wo_{0.7}\ En_{98.9}$), silica and troilite (Fig. 3c-d). Silica apparently occurs mainly along the edges of the diopside grains in the chondrule. The troilite in this chondrule contains 0.4 wt. % Ti and 0.4 Cr, as is typical of troilite in enstatite chondrites (e.g., Keil, 1968).

Metal nodules in EL3 chondrites (also called metal-silicate intergrowths) have been a subject of controversy as to whether they are primary, nebula-formed objects or products of impact melting. EH3 chondrites also contain metal-rich objects with assemblages of sulfides, phosphide, graphite and silicates (Weisberg and Prinz, 1998; Lehner et al., 2010) and have been referred to as

metal-sulfide nodules (MSN). The EL3 nodules contain laths of enstatite (~En_{98}) intergrown with metal. We studied one metal-rich nodule (M5) in ALH 81189 and three metal-rich nodules (M1-2, M8, and M10) in MAC 88136 (Figs. 4a-d). In the MAC 88136 EL3 chondrite, enstatite occurs mainly as laths, needles and irregular crystals within the metal. In the metal nodule in ALH 81189 studied here, the enstatite occurs as anhedral crystals oriented around metal in the center, forming what appears to be a discontinuous enstatite-rich layer (Fig. 4b).

Compositions of most silicates we analyzed are reduced enstatite (En>98) and forsterite (Fo>98) with a few exceptions such as C9 in ALH 81189 discussed above. Fig. 5 shows the distribution of silicate compositions in the sections studied.

Oxygen isotopes

Our new data for the average oxygen isotope ratios for each object we studied are given in Table 1 (complete dataset is in appendix) and plotted in Fig. 6 along with literature chondrule data from E chondrites. While whole rock E chondrites plot along the terrestrial fractionation (TF) line (e.g., Weisberg and Kimura, 2012), the majority of olivine and pyroxene analyses plot along the slope~1 PCM line, with most data clustering at the intersection of the PCM with the TF line (Fig. 6a). The mean oxygen isotope ratios of individual chondrules were determined for most of the chondrules that show internally homogeneous oxygen isotopic ratios (Fig. 6b).

Two PP chondrules show a significant range of internal variability (Fig. 6c). ALH 81189 C1 contains ^{16}O-rich relict olivine grains that reach $\delta^{18}O$ and $\delta^{17}O \sim -30‰$, in contrast to those of pyroxene in the same chondrule that plot above the TF line. ALH 85159 C51 shows the highest $\delta^{18}O$ and $\delta^{17}O$ values among all of the chondrule studied and shows significant internal variability from 6‰ to 8‰ and from 4‰ to 6‰, respectively. Olivine in the AOA from ALH 81189 is ^{16}O-

257 rich with $\delta^{18}O$ = –46.5‰, $\delta^{17}O$ = –48.0‰, similar to AOAs and refractory inclusions in other
258 chondrite groups (Fig. 6c; e.g., Krot et al., 2004).

259 The individual chondrule data from ALH 81189 and ALH 85159 (EH3) and the more limited
260 data set from MAC 88136 (EL3) overlap and show a similar distribution. The $\Delta^{17}O$ for ALH 81189
261 and paired ALH 85159 chondrules range from –1.4 to 1.3‰ and for MAC 88136 the range is
262 slightly smaller at –0.6 to 1.3‰. Olivine-rich chondrules (PO, BO, POP) tend to plot on and below
263 the TF line, while more PP chondrules plot above the TF line, as indicated from the distribution of
264 individual olivine and enstatite data in Fig 6a. The PP chondrule (C22) in ALH 81189 has the most
265 ^{16}O-rich mean oxygen isotope ratios ($\delta^{18}O$ = 2.3‰, $\delta^{17}O$ = –0.2‰). Petrologically, C22 is a
266 porphyritic pyroxene chondrule dominated by enstatite. The only petrologic difference between
267 C22 and other chondrules in ALH 81189 is that C22 has a slightly higher amount of Al-rich
268 mesostasis. The unusual diopside-rich chondrule in MAC 88136, and enstatite in the metal-rich
269 nodules in both EH3 and EL3 all show oxygen isotopic ratios within a similar range of other
270 chondrules. Silica from the silica-rich chondrule (C30) and the average of two analyses of silica
271 in the diopside-rich chondrule (C1; Fig. 3b) in MAC 88136 are also plotted in Fig. 6b. They are
272 compositionally similar, plotting on the TF line at $\delta^{18}O$ = 8.7‰ and 8.3‰, respectively toward
273 much more ^{16}O-poor compositions than olivine and pyroxene.

274 The data from most chondrules and other objects in ALH 81189, ALH 85159 and MAC 88136
275 form a regression line $\delta^{17}O = (0.88\pm0.10)\times\delta^{18}O - (2.1\pm0.5)$ that is statistically indistinguishable
276 from the slope~1 PCM line, $\delta^{17}O = (0.987\pm0.013)\times\delta^{18}O - (2.70\pm0.11)$ (Fig. 6d). Four chondrules
277 from ALH 81189 and one from MAC 88136 appear to suggest a resolvable second trend above
278 the PCM line (referred to as "other chondrules" in Fig. 6d). They show indistinguishable $\Delta^{17}O$
279 values ~ 0.9‰ (Fig. 6b) and may plot along the slope ~0.5 line (Fig. 6b). However, they comprise

a linear trend with two heterogeneous chondrules, ALH 85159 C51 and three moderately ^{16}O-rich relict olivine grains from ALH 81189 C1 (Fig. 6d). A regression line through these data form a slightly shallower slope –0.84±0.04 with an intercept of –1.0±0.2‰ (Fig. 6d). This second trend significantly overlaps with the chondrule data from LL chondrites (Kita et al. 2010). To check whether these two groups truly belong to two distributions in the two-dimensional space δ^{18}O-δ^{17}O, we performed a two-dimensional, two samples Kolmogorov-Smirnov test. This test is a non-parametric test that computes the probability that two samples belong to the same distribution by comparing their cumulative distributions. In this case, the test returns a P-value of 7.1×10^{-5}, well below the accepted threshold of 0.05 to reject the hypothesis, allowing us to conclude that these two trends are in fact two separate trends.

The data distribute in a similar range to those from our previous study of the Sahara 97096 and Yamato-691 EH3 and the anomalous LEW 87223 chondrite (Weisberg et al., 2011; Fig. 6e). The new dataset is also similar to the individual chondrule data reported by Clayton and Mayeda (1985) and Tanaka and Nakamura (2017), which are shown in Fig. 6e for comparison. In Fig. 6f, a regression line of all E3 chondrules is obtained by using these literature data and all data obtained in this study. The regression line gives $\delta^{17}O = (0.997\pm0.025)\times\delta^{18}O - (2.40\pm0.2)$, which is almost identical to the PCM line, but has a large MSWD of 24, reflecting two separate trends at the higher δ^{18}O and δ^{17}O ends.

Type I chondrules in some C chondrite groups show a trend of Δ^{17}O increasing with decreasing Mg# for type I chondrules, whereas such a trend is not observed for chondrules in O and R chondrites (Kita et al., 2010, 2015). The data for the E3 chondrules do not show a clear trend (Fig. 7). A regression line through the data (r=0.2) shows a very slight hint of Δ^{17}O decreasing with the average Mg# for the chondrule silicates but it is not statistically significant.

Discussion

Relationship between chondrules, metal-rich nodules and refractory inclusions in EH3 and EL3 chondrites.

The oxygen isotopic compositions of the silicates within most chondrules analyzed in this study appear to be fairly uniform. Weisberg et al. (2011) specifically selected olivine-bearing chondrules and, as a result discovered oxygen isotopic heterogeneity in minerals from some individual chondrules in EH3 chondrites and suggested incomplete melting of the chondrules, survival of minerals from previous generations of chondrules, chondrule recycling, or possibly open system behavior during chondrule formation, as proposed for chondrules in O and C chondrites. Weisberg et al. (2011) found one chondrule in Sahara 97096 that contained an olivine grain with an R chondrite-like oxygen isotopic composition. They interpreted this to be a relict grain, suggesting limited mixing of materials from other reservoirs and the close proximity of E, O and R chondrite precursors, compared to C chondrites. This is consistent with recent discoveries of whole rock nucleosynthetic isotopic differences between non-carbonaceous (including E, O and R) and carbonaceous chondrites (Trinquier et al., 2009).

Overlap in oxygen isotopic compositions between EH3 and EL3 chondrules suggests that they share similar precursors but the mineral assemblages and compositions (e.g., higher Si content in EH metal) in EH3 and EL3 indicate different degrees of reduction (Keil, 1968; Weisberg and Kimura, 2012), suggesting differences in their nebular environments and/or separate, possibly multiple parent bodies (e.g., Weyrauch, 2018). Most of the components that we analyzed show similar oxygen isotopic compositions, including the chondrules and enstatite and forsterite mineral fragments, enstatite in metal-rich nodules and the silicates with more FeO-rich compositions. This

is consistent with previous studies that showed that the less common FeO-bearing minerals in E3 chondrites share the same oxygen isotopic compositions as the more common, reduced, FeO-poor olivine and pyroxene in E3's (Weisberg et al., 2011, Kimura et al., 2003). Additionally, the unusual diopside-plagioclase fragment (F9; Fig. 3a) in ALH 81189 and the large diopside-enstatite chondrule (C1; Figs. 3c-d) in MAC 88136 also have similar isotopic compositions to the other E3 components. Thus, all of these objects likely formed from the same mix of precursors and were likely molten or partially molten and exchanged oxygen in the same, presumably chondrule-forming, region.

Derivation of the FeO-bearing silicates from the same oxygen reservoirs as the more reduced silicates and textural and compositional evidence indicating that the FeO-bearing silicates have undergone various degrees of reduction (Rambaldi et al. 1983; Lusby et al. 1987; Weisberg et al. 1994; Kimura et al. 2003; Weisberg et al. 2011), suggest a stage of more oxidizing conditions in the evolution of enstatite chondrites. This is consistent with studies of element valence states that also suggest E chondrites were originally more oxidized at some point in their history (e.g., Jacquet et al., 2015; Simon et al., 2016).

The origin of the metal-rich nodules in E3 chondrites has been controversial. There are four major, conflicting hypotheses for the origin of these nodules in EL3 chondrites: (1) the metal-rich nodules are products of impact melting and formed by mobilization and injection of metal into pores in the EL3 regolith (Van Nierkerk and Keil, 2011), (2) metal-rich nodules are pre-accretionary and resulting from impact disruption of early differentiated bodies (Horstmann et al., 2014), (3) the nodules are chondrule-like melts formed in the early solar system (Weisberg et al., 2013; Ebel and Sack, 2013), and (4) the nodules are aggregates of condensates (El Goresy et al., 2017; Lin et al., 2011). Kadlag et al. (2019) measured Si isotopes in silicates and metal in an EH3

chondrite and showed differences in their Si isotopic compositions suggesting that the differences were inherited from different nebular reservoirs. However, Si isotope fractionation between silicate and metal may also be responsible for the differences. Based on major and trace element analyses, Lehner et al. (2014) concluded that the matrix, chondrule, and metal-sulfide nodule compositions are apparently complementary, suggesting all the components of the EH3 chondrites came from the same nebular reservoir.

The oxygen isotopic data can help shed light on the origin of the EL3 nodules. The nodules in the EL3 chondrites have irregular to near-spherical shapes and characteristically contain enstatite laths or needles intergrown with the metal (Figs. 4c and d). Their sharp boundaries with surrounding matrix and other objects suggest the nodules formed as free-floating objects similar to the chondrules. They may be aggregates of condensates or were molten or partially molten. For the limited number of metal-rich nodules we were able to analyze, the oxygen isotopic ratios (as well as the mineral compositions) of the enstatite laths in the metal-rich nodules are similar to those of enstatite in the silicate (metal-free) chondrules. Additionally, the metal-rich nodule and chondrule silicates all plot along the same (PCM) mixing line defined by the highly primitive Acfer 094 C chondrite. Although we cannot conclusively determine the origin of the metal-rich nodule silicates, the petrologic and oxygen data are more consistent with formation of the metal-rich nodules prior to chondrite accretion, in an environment similar to the coexisting chondrules, and forming from a process similar to that which formed the metal-free chondrules, but from more metal-rich mixtures of precursors.

The separation of the metal and silicates in chondrites is not well understood. Metal-rich nodules may have been spatially or temporally separated from the metal-poor chondrules, possibly due to an aerodynamic or a magnetic sorting mechanism that resulted in local metal-rich and metal-

depleted regions that contributed to the same parent body (e.g., Hubbard, 2016). Weisberg et al. (2013) suggested a fractional condensation model to account for earlier formed (higher temperature) metal-rich "chondrule" compositions. Metal condenses at higher temperatures (1375 K) than silicate (olivine, diopside and enstatite condense at 1100, 1050 and 950 K, respectively) in a nebular reservoir with a C/O ratio greater than 1 at 10^{-3} bar total pressure (Ebel, 2006, Plate 9). Thus, it is reasonable to consider the metal-rich nodules in E3 chondrites as essentially "metal-rich chondrules", as suggested by Gooding and Keil (1981) and Alpert et al. (2020) for ordinary chondrites.

The Enstatite Chondrite Mixing Line and the PCM line

Although the whole rock oxygen isotopic compositions for E chondrites plot along or close to the TF line on a three isotope diagram (Clayton and Mayeda, 1984, 1999; Weisberg et al., 1995, 2011, Weisberg and Kimura, 2012), the individual chondrules, mineral fragments and metal-rich nodules form a trend toward more ^{16}O-rich compositions, (Fig. 6a, b), consistent with our previous studies of chondrules in E3 chondrites (Weisberg et al., 2011). This trend is also supported by the findings of Tanaka and Nakamura (2017), though they suggested their data formed a somewhat steeper slope. Weisberg et al. (2011) referred to the array of E3 chondrite oxygen isotopic ratios as the enstatite chondrite mixing line (ECM) but acknowledged that this mixing line is statistically indistinguishable from the slope-1 trend defined by chondrules from the primitive C chondrite Acfer 094 and referred to as the primitive chondrite mineral line (PCM) by Ushikubo et al. (2012).

Our data indicate a clear distinction between chondrules in the E chondrites and those in the LL chondrules which form a slope-0.5 trend mostly above the terrestrial fraction (TF) line with LL chondrules plotting to the left of the PCM (Kita et al., 2010). E chondrite chondrules differ from

whole rock R chondrites which form a trend at even higher, ^{17}O-rich values (e.g., Bischoff et al., 2011) and R chondrite chondrules, which overlap with ordinary chondrite chondrules (Kita et al., 2015). The E3 chondrules are also isotopically different from CV and CM chondrite groups, which form a trend apparently parallel to but below the PCM line (Fig. 8). Chondrules from CR and EC chondrites plot closer to the PCM line than other chondrite groups (Fig. 8).

The PCM line is a regression line for individual SIMS olivine and pyroxene analyses from the Acfer 094 ungrouped C chondrite, including relict olivine and chondrules with internally heterogeneous oxygen isotopic ratios (Ushikubo et al., 2012). Chondrule data from other C chondrites generally plot on the PCM line (Rudraswami et al. 2011; Tenner et al. 2013; 2015; Marrocchi et al., 2018, 2019). The PCM line is interpreted to represent a mixing trend of two extreme primary oxygen isotope reservoirs of solids in the early solar system that potentially accreted to form the terrestrial planets, including the Earth (Ushikubo et al., 2012). It has been recognized that a small fraction of chondrules in carbonaceous chondrites, including Acfer 094, show OC-like oxygen isotopic ratios, which plot near the TF line (Δ^{17}O~0‰) but left of the PCM line in oxygen three isotope space (Tenner et al. 2017; Hertwig et al. 2018; 2019a; 2019b). On the contrary, chondrule analyses from CV and CM chondrites (Hertwig et al. 2018; 2019b; Chaumard et al. 2018; 2021), which are with slightly better precisions compared to earlier studies, are offset slightly from the PCM line, to the right. Recently, Williams et al. (2020) observed that oxygen isotope ratios of CV chondrite chondrules show two linear trends that are related to their ε^{50}Ti and ε^{54}Cr abundances. Chondrules with positive ε^{50}Ti and ε^{54}Cr plot with constant offset below the PCM line and chondrules with negative ε^{50}Ti and ε^{54}Cr plot towards OC chondrule compositions. These chondrule populations might have formed in the outer and inner protoplanetary disk, respectively. Thus, the PCM line might represent an average of the two trends found by Williams

et al. (2020). Schneider et al. (2020) also reported ε^{50}Ti and ε^{54}Cr values of chondrules in several chondrite groups including CV, but did not find negative ε^{54}Cr anomalies from chondrules in CV. However, their CV chondrite chondrule data were limited to the dominant type I chondrules with negative Δ^{17}O. Kita et al. (2010) argued that condensation of olivine from high temperature gas could have resulted in deviation of oxygen isotopes to the left of the PCM line. Contribution of such fractionated precursors could have been much less abundant among the chondrule precursors for E chondrites than in other chondrite groups..

The distribution of chondrules along the PCM line is different between the E3 chondrules and the CR chondrules (Fig. 8). Chondrules from CR and Acfer 094 extend toward more ^{16}O-rich compositions (Ushikubo et al., 2012; Schrader et al., 2013, 2014, 2017; Tenner et al., 2015) while the E3 chondrules mainly form a tighter cluster of data points closer to the TF line (zero in Fig. 8) and E3 whole rock. One possible explanation for this difference is that the amount of ^{16}O-rich refractory material that was mixed into the E3 chondrule-forming region was less than that in the carbonaceous chondrite chondrule forming regions. This may be recorded in the very low abundance of CAIs and AOAs in the E3 chondrites (e.g., Guan et al., 2000; Fagan et al., 2001; Lin et al., 2003). Of the 3 thin sections studied, we found only one AOA. Additionally, this interpretation is supported by the relatively lower Ca/Si and Al/Si ratios of E chondrites relative to other chondrite groups (e.g., Hutchison et al., 2005), and their depletion in refractory lithophile trace elements (Dauphas and Pourmand, 2015). The suggestion of refractory material as chondrule precursors is also consistent with the findings of Jacquet and Marrocchi (2017) that chondrules show recognizable subdued group II REE patterns, presumably inherited from a refractory precursor.

Thus, we propose that a similar pool of chondrule precursors were distributed to the different (C, carbonaceous, and E, non-carbonaceous) chondrule forming regions in the protoplanetary disk but with different amounts of ^{16}O-rich refractory materials, prior to development of the postulated *Jupiter divide* (e.g., Warren, 2011; Kruijer et al., 2017). Such an interpretation would be consistent with recent measurements of individual chondrules in C chondrites (Williams et al., 2020). Williams et al. (2020) suggested the Jupiter barrier was inefficient allowing chondrules to move from the inner disk to the outer disk at 2-3 Ma after CAI formation. Additionally, Schrader et al. (2020) showed that dusty olivine chondrules in O and C chondrites have O-isotope compositions that match those of UOC chondrule olivine ($\Delta^{17}O \sim 0‰$), suggesting an origin from a UOC source. They suggested that UOC chondrules and/or chondrule fragments migrated from the inner Solar System outwards to CM chondrite chondrule-forming region, beyond the orbit of Jupiter.

Alternatively, the range of E3 oxygen isotopes could reflect addition of heavy isotopes in more volatile precursor material (e.g., cosmic symplectite and/or organic matters, Sakamoto et al., 2007; Hashizume et al. 2011). The $\Delta^{17}O$ values of non-carbonaceous chondrites correlates with the "oxygen excess" values calculated by the amounts of iron oxide and phosphates (Alexander et al., 2019) and a positive correlation was found for $\Delta^{17}O$ and Mg # for type I chondrules in CR chondrites (Tenner et al., 2015). These data suggest that the amount of H_2O may also an important factor in controlling the $\Delta^{17}O$ values of chondrules. Thus, $\Delta^{17}O$ of chondrules in carbonaceous chondrite groups may be partially controlled by interaction with water. However, E chondrites have relatively low abundances of H_2O and do not show a positive relationship between Mg# and $\Delta^{17}O$, as in the carbonaceous chondrites.

The trend in E3 chondrule oxygen has also been interpreted to result from reactions between ^{16}O-rich, olivine-rich chondrule melts and ^{16}O-poor SiO-rich gas (Tanaka and Nakamura, 2017).

463 Tanaka and Nakamura (2017) suggested that such reactions may explain the oxygen isotopic
464 systematics, by adapting the model presented by Marrocchi and Chaussidon (2015), as well as the
465 reduced and silica-saturated compositions of E chondrite chondrules. They reported a slope of 1.27
466 for their oxygen isotopic compositions. In the Marrocchi and Chaussidon (2015) model, the
467 systematic oxygen isotopic variations in C chondrite chondrules result from open-system gas–melt
468 exchanges during chondrule formation. In their model, the PCM line does not correspond to a
469 mixing line between two discrete reservoirs but instead records the signature of high-temperature
470 interactions between nebular gas and dust (of CI composition and plotting on the carbonaceous
471 chondrite anhydrous mineral [CCAM] line) produced in the accretion disk. Tanaka and Nakamura
472 (2017) used the same model with slightly different endmember oxygen isotope ratios to explain
473 the observed EH3-4 chondrule data that plot along the line with the slope >1. However, the slope-
474 1.27 line estimated by Tanaka and Nakamura (2017) is based on data that includes enstatite
475 chondrites more equilibrated than type 3. For their unequilibrated chondrites (EH3), they report 6
476 individual chondrules and 13 data points that are from composite chondrules or enstatite separates.
477 A regression line through their unequilibrated chondrite data, the EH3 data from Weisberg et al.,
478 (2011) and our new data here are not distinguishable from a slope-1 line.
479 Gas-melt interactions during chondrule formation has been cited as a major factor in producing
480 the petrologic features of chondrules (Ebel et al., 2018). Marrocchi and Libourel (2013) argued
481 that the sulfur content of chondrules is dependent on the fS_2 and fO_2 of the surrounding gas. Using
482 cathodoluminescence (CL) Libourel and Portail (2018) documented internal zoning of chondrule
483 olivine and interpreted it as evidence for high-temperature gas-assisted near-equilibrium epitaxial
484 growth of the olivine during chondrule formation. Jacquet et al., (2020) identified CL zoning in
485 isolated olivine grains as a signature of decreasing refractory element concentrations toward the

margins of grains, and took it to be evidence of interaction of the grains with the surrounding gas. For enstatite chondrites, Piani et al. (2016) suggest that most of the sulfides found in EH3 chondrite chondrules are magmatic minerals that formed after the diffusion of S from a volatile-rich gaseous environment into the molten chondrules. Additionally, sulfidation of silicates has been proposed as the mechanism for formation of Niningerite in EH3 chondrites (e.g., Rubin 1983; Lehner et al., 2013). Thus, open system behavior may have also played a role in establishing the oxygen isotopic compositions of E3 chondrules.

In the oxygen isotope exchange model proposed by Marrocchi and Chaussidon (2015) for carbonaceous chondrites, they consider evaporation of CI chondritic dust that contains much more C and H compared to E chondritic materials. If the ambient gas during E chondrite chondrule formation was depleted in H_2O and CO molecules and enriched in SiO, gas-melt oxygen isotope exchange would produce negligibly small mass dependent fractionation in chondrule melts, due to small equilibrium fractionation between silicate and SiO gas (e.g., 0.39‰ at 1600K between pyroxene and SiO gas; Javoy 2012). This is consistent with the observed slope ~1.0 regression line determined from the E3 chondrule data presented in Fig. 6f.

A second trend?

Data from seven of the chondrules analyzed here form a separate trend above the PCM line. These oxygen isotopic compositions overlap those of some OC chondrules (Kita et al., 2010) but extend toward more ^{16}O-poor compositions (Fig. 6d). These chondrules have reduced (Mg-rich) silicate compositions and are petrologically similar to other chondrules in ALH 81189. The trend may be the result of limited mixing between the different oxygen reservoirs. Substantial overlap between the second group chondrule data and LL chondrite chondrules (Fig. 6d) may suggest some

509 mixing of OC-like precursors in E chondrite forming regions. Weisberg et al. (2011) found
510 enstatite in Sahara 97096 with oxygen isotopic ratios that plotted within the field for ordinary
511 chondrite chondrules and a relict grain within a chondrule that had a ^{17}O-rich composition similar
512 to R chondrites. They concluded that there was transport and some mixing of the materials thought
513 to have formed inside of Jupiter, i.e., the O, R and E chondrite reservoirs.
514
515 *Significance of the oxygen isotopic composition of silica*
516 The common occurrence of silica in chondrules and Si in metal in enstatite chondrites, a
517 result of their silica-saturated compositions, is one of the characteristic features that distinguish E
518 chondrites from the other chondrite groups. Silica grains from two different objects (a silica-rich
519 and a diopside-rich chondrule) in MAC 88136 are isotopically similar, plotting on the TF line at
520 $\delta^{18}O$ = 8.7‰ and 8.3‰, respectively, and have different oxygen isotope compositions than the
521 olivine and pyroxene in the same chondrules (Fig. 6b). Additionally, the silica plots further up the
522 TF line relative to whole rock compositions (Fig. 6a, b). Thus, they potentially mass balance the
523 more ^{16}O-rich compositions of some chondrules to yield the whole rock composition.
524 Kimura et al. (2005) studied silica polymorphs as a mechanism to understand the thermal
525 histories of E chondrites. They reported cristobalite and tridymite in chondrule mesostases con-
526 sistent with silica as the liquidus phase after crystallization of enstatite, and consistent with melting
527 and rapid crystallization rates for the chondrules. As the last crystallizing phase, silica may have
528 exchanged oxygen with and preserved the composition of the ambient nebular gas. It is also pos-
529 sible that silica condensed from a late stage SiO-rich nebular gas as suggested for silica-rich rims
530 on some chondrules in CR chondrites (Krot et al., 2004). The silica could also form by reduction
531 of Fe from FeO-bearing silicates as observed in some chondrules in unequilibrated E chondrites

(e.g., Weisberg et al., 1994). However, FeO-bearing silicates have oxygen isotopic compositions similar to enstatite and forsterite in the chondrules (e.g., Kimura et al., 2003). Thus, reduction reactions would not explain the observed oxygen isotopic compositions of the silica.

In the case of MAC 88136 C1, the $\Delta^{17}O$ of the silica grains are indistinguishable from those of pyroxene in the same chondrule, but the $\delta^{18}O$ of silica grains are ~3‰ higher than pyroxene, which corresponds to a temperature of equilibrium at 600-700˚C using oxygen isotope thermometry (Clayton and Kieffer, 1991; Javoy et al., 2012). However, this temperature seems to be too low if the silica is a high temperature polymorph (as found for chondrule silica by Kimura et. al., 2005). Alternatively, silica acquired higher $\delta^{18}O$ during low temperature parent body heating because of its fast oxygen isotope diffusion rate compared to olivine and pyroxene (e.g., Cole and Chakraborty, 2001). The difference in $\delta^{18}O$ may also be the result of applying the instrumental bias of quartz to correct for cristobalite. The difference in bias between quartz and cristobalite has not been evaluated but the $\Delta^{17}O$ values are not affected (Ushikubo et al., 2012).

Conclusions

1) The oxygen isotopic compositions of the silicates in most of the E3 chondrules are fairly uniform within each chondrule, with a few exceptions.

2) The oxygen isotopic compositions in EH3 and EL3 chondrules overlap, suggesting that they share similar precursors but the mineral assemblages and compositions in EH3 and EL3 indicate different degrees of reduction (e.g., Keil, 1968; Weisberg and Kimura, 2012), suggesting differences in their nebular environments and/or separate, possibly multiple (e.g., Weyrauch, et al., 2018), parent bodies.

555

556 3) The limited metal-rich nodules we analyzed have oxygen isotopic ratios (as well as mineral
557 compositions) similar to the silicate (metal-free) chondrules. This is consistent with formation of
558 the metal-rich nodules prior to chondrite accretion, in an environment similar to the coexisting
559 chondrules, and their forming from a process similar to that which formed the metal-free
560 chondrules, but from more metal-rich mixtures of precursors.

561

562 4) Our data indicate a clear distinction between chondrules in the E chondrites and those in the LL
563 or R chondrules. E chondrite chondrules also differ from CV and CM chondrite groups, which
564 form a trend parallel to but below the PCM line. The chondrules from CR and E3 chondrites plot
565 closer to the PCM line than all other chondrite groups.

566

567 5) The distribution of chondrules along the PCM line is different between the E3 chondrules and
568 the CR chondrules, with CR chondrules extending toward more ^{16}O-rich compositions (Schrader
569 et al., 2013, 2014, 2017; Tenner et al., 2015) while the E3 chondrules mainly form a tighter cluster
570 of data points closer to the TF line near E3 whole rocks. A possible explanation is that a smaller
571 amount of ^{16}O-rich, refractory material was mixed into the E3 chondrule-forming region than that
572 into the carbonaceous chondrite chondrule-forming regions. Thus, we propose that similar pools
573 of chondrule precursors were distributed to the different (C, carbonaceous, and E, non-
574 carbonaceous) chondrule forming regions in the protoplanetary disk but with different amounts of
575 ^{16}O-rich refractory materials, prior to development of the postulated *Jupiter divide* (e.g., Warren,
576 2011; Kruijer et al., 2017) and/or the Jupiter divide was inefficient in separating these materials
577 (e.g., Williams et al., 2020).

6) Data from seven of the EC chondrules analyzed appear to form a separate trend above the PCM line.

7) The PCM line might represent an average of the two oxygen isotope trends that Williams et al. (2020) observed in CV chondrules, which they related to their ε^{50}Ti and ε^{54}Cr abundances. Kita et al. (2010) argued that condensation of olivine from high temperature gas could have resulted in deviation of oxygen isotopes to the left of the PCM line. Contribution of such fractionated precursors could have been much less significant among the chondrule precursors for E chondrites, explaining why the EC chondrules plot closer to the PCM line than some of the other chondrite groups.

Acknowledgements: This material is based upon work partially supported by the National Aeronautics and Space Administration under grants #80NSSC18K0589 (MKW), and NNX16AD37G (DSE) issued through the Emerging Worlds program. AMNH staff provided invaluable assistance, including M. Chase, A. Smith, and C. Martin and Kingsborough CUNY staff including Robert Schenck. WiscSIMS is partly supported by NSF (EAR 1658823).

References:

Alexander C. M. O'D. (2019) Quantitative models for the elemental and isotopic fractionations in the chondrites: The non-carbonaceous chondrites. *Geochimica et Cosmochimica Acta* **254**, 246–276.

Alpert S. P., Ebel D. S., Weisberg M. K. and Neiman J. (2020) Petrology of the opaque assemblages in unequilibrated ordinary chondrites. *Meteoritics and Planetary Science*, MAPS 3457 in press. doi: 10.1111/maps.13619

Bischoff A., Vogel N., and Roszjar J.(2011) The Rumuruti chondrite group. *Chemie der Erde* **71**, 101-133.

Boesenberg J. S., Young E. D., Ziegler K. and Hewins R. H. (2005) Evaporation and the absence of oxygen isotopic exchange between silicate melt and carbon monoxide gas at nebular pressures. *Meteoritics and Planetary Science Suppl*. **40**, A22.

Burbine T. H., McCoy T. J., Nittler L. R., Benedix G. K., Cloutis E. A. and Dickenson T. L. (2002) Spectra of extremely reduced assemblages: Implications for Mercury. *Meteoritics and Planetary Science* **37**, 1233-1244.

Chaumard N., Defouilloy C. and Kita N. T. (2018) Oxygen isotope systematics of chondrules in the Murchison CM2 chondrite and implications for the CO-CM relationship. *Geochimica et Cosmochimica Acta* **228**, 220–242.

Chaussidon M., Libourel G. and Krot A. N. (2008) Oxygen isotopic constraints on the origin of magnesian chondrules and on the gaseous reservoirs in the early Solar System. *Geochimica et Cosmochimica Acta* **72**, 1924–1938.

625 Clayton R. N. and Kieffer S. W. (1991) Oxygen isotopic thermometer calibrations. *Geochemical*
626 *Society, Special Publication* **3**, pp.3–10.
627
628 Clayton R. N. and Mayeda T. K. (1984) Oxygen isotopic compositions of enstatite chondrites and
629 aubrites. *Journal Geophysical Research* **89**, C245–C249.
630
631 Clayton R. N. and Mayeda T. K. 1985. Oxygen isotopes in chondrules from enstatite chondrites:
632 Possible identification of a major nebular reservoir (abstract). 16th Lunar and Planetary Sci-
633 ence Conference 142–143.
634
635 Clayton R. N., and Mayeda T. K. (1999) Oxygen isotope studies of carbonaceous chondrites'.
636 *Geochimica et Cosmochimica. Acta* **63**, 2089–2104.
637
638 Cole D. R. and Chakraborty S. (2001) Rates and Mechanisms of Isotopic Exchange. *Reviews in*
639 *Mineralogy and Geochemistry* **43,** 83–223.
640
641 Dauphas, N. (2017) The isotopic nature of the Earth's accreting material through time. *Nature* **541,**
642 521–524.
643
644 Dauphas N. and Pourmand A. (2015) Thulium anomalies and rare earth element patterns in
645 meteorites and Earth: Nebular fractionation and the nugget effect, *Geochimica et*
646 *Cosmochimica Acta* **163**, 234-261.
647

El Goresy et al. A., Lin Y., Miyahara M., Gannoun A., Boyet M., Ohtani E., Gillet P., Trieloff M., Simionovici A., Feng L., and Lemelle L. (2017) Origin of EL3 chondrites: Evidence for variable C/O ratios during their course of formation—A state of the art scrutiny. *Meteoritics and Planetary Science* **52**, 781-806.

Ebel D. S. (2006) Condensation of rocky materials in astrophysical environments. In *Meteorites and the Early Solar System **II***, D. Lauretta, H.Y. McSween Jr., eds., University Arizona, Tucson, pp. 253-277.

Ebel, D. S., Alexander C. M. O'D. and Libourel G. (2018) Vapor-melt exchange - Constraints on chondrule formation conditions and processes. *In Chondrules: Records of Protoplanetary Disk Processes*. Eds. S. Russell, A. Krot and H. C. Connolly Jr. Cambridge U. Press. pp. 151-174.

Ebel D. S. and Sack R. O. (2013) Djerfisherite: Nebular source of refractory potassium. *Contributions to Mineralogy and Petrology* **166**, 923-934.

Ebel D. S. and Stewart S. T. (2018) The elusive origin of Mercury. In *Mercury: The View after MESSENGER*. C. Solomon, B. J. Anderson and L. R. Nittler (editors), pp. 497-515. Cambridge: Cambridge University Press.

Fagan T., McKeegan K. D., Krot A. N., Keil K. (2001) Calcium-aluminum-rich inclusions in enstatite chondrites (II): Oxygen isotopes. *Meteoritics and Planetary Science* **36**, 223-230.

671 Fitoussi C. and Bourdon B. (2012) Silicon isotope evidence against an enstatite chondrite earth.
672 *Science* **335**, 1477–1480.
673
674 Gooding, J. L. and Keil K. (1981) Relative abundances of chondrule primary textural types in
675 ordinary chondrites and their bearing on conditions of chondrule formation. *Meteoritics* **16**,
676 17-42.
677
678 Gray M. L., Weisberg M. K., Ebel D. S., Alexander C. M. O'D., Howard K. T. (2021) Abundances
679 and isotopic compositions of volatiles (H, N, C) in unequilibrated enstatite chondrites and the
680 volatile inventories of the terrestrial planets. *Lunar and Planetary Science Conference* **52**, ab-
681 stract # 2116.
682
683 Grossman L. and Steele I.M. (1976) Amoeboid olivine aggregates in the Allende meteorite. *Geo-*
684 *chimica et Cosmochimica Acta* **43**, 817-829.
685
686 Guan Y., Huss G. R., MacPherson G. J. and Wasserburg G. J. (2000) Calcium-aluminum-rich
687 inclusions from enstatite chondrites: Indigenous or foreign? *Science* **25**, 1330-1333.
688
689 Hashizume K., Takahata N., Naraoka H. and Sano Y. (2011) Extreme oxygen isotope anomaly
690 with a solar origin detected in meteoritic organics. Nature Geosci. 4, 165–168.
691

692 Hertwig A., Defouilloy C. and Kita N. T. (2018) Formation of chondrules in a moderately high
693 dust enriched disk: evidence from oxygen isotopes of chondrules from the Kaba CV3 chon-
694 drite. *Geochimica et Cosmochimics. Acta* **224**, 116–131.
695
696 Hertwig A. T., Kimura M., Ushikubo T., Defouilloy C. and Kita N. T. (2019a) The 26Al- 26Mg
697 systematics of FeO-rich chondrules from Acfer 094: Two chondrule generations distinct in age
698 and oxygen isotope ratios. Geochimica et Cosmochimica Acta 253, 111- 126.
699
700 Hertwig A., Kimura M., Defouilloy C. and Kita N. T. (2019b) Oxygen isotope systematics of
701 chondrule olivine, pyroxene, and plagioclase in one of the most pristine CV3Red chondrites
702 (Northwest Africa 8613). *Meteoritics and Planetary Science* **54**, 2666-2685.
703
704 Horstmann M., Humayun M., and Bischoff A. (2014) Clues to the origin of metal in Almahata
705 Sitta EL and EH chondrites and implications for primitive E chondrite thermal histories.
706 *Geochimica et Cosmochimica Acta* **140**, 720–744.
707
708 Hubbard A. (2016) Ferromagnetism and particle collisions: Applications to protoplanetary disks
709 and the meteoritical record. *Astrophysical Journal* **826**, 152-162.
710
711 Hutchison R., Bridges J. C. and Gilmour J. D. (2005) Chondrules: Chemical, Petrographic and
712 Chronologic Clues to Their Origin by Impact. In: *Chondrites and the Protoplanetary Disk,*
713 *ASP Conference Series*, **341**, 2005, A. N. Krot, E. R. D. Scott, & B. Reipurth, eds.
714

715 Jacquet E., Alard O.and Gounelle M. (2015) The formation conditions of enstatite chondrites:
716 Insights from trace element geochemistry of olivine-bearing chondrules in Sahara 97096
717 (EH3). *Meteoritics and Planetary Science* **50**, 1624–1642.
718 Jacquet E. and Marrocchi Y. (2017) Chondrule heritage and thermal histories from trace element
719 and oxygen isotope analyses of chondrules and amoeboid olivine aggregates. *Meteoritics and*
720 *Planetary Science* **52**, 2672-2694.
721
722 Jacquet E., Piralla M., Kersaho P. and Marrocchi Y. (2020) Origin of isolated olivine grains in
723 carbonaceous chondrites. *Meteoritics and Planetary Science*, in press. doi:
724 10.1111/maps.13583.
725
726
727 Javoy M. (1995) The intergral enstatite chondrite model of the earth. *Geophysical Research Letters*
728 **22**, 2219-2222.
729
730 Javoy M., Balan E., Méheut M., Blanchard M., and Lazzeri M. (2012) First-principles investiga-
731 tion of equilibrium isotopic fractionation of O- and Si-isotopes between refractory solids and
732 gases in the solar nebula. *Earth and Planetary Science Letters* **319–320**, 118-127.
733
734 Javoy M., Kaminski E., Guyot F., Andrault D., Sanloup C., Moreira M., Labrosse S.,Jambon A.,
735 Agrinier P., Davaille A., Jaupart C., (2010) The chemical composition of the Earth: Enstatite
736 chondrite models, *Earth and Planetary Science Letters* **293**, 259-268.
737

738 Jones R. H., Leshin L. A., Guan Y. B., Sharp Z. D., Durakiewicz T. and Schilk A. J. (2004) Oxygen
739 isotope heterogeneity in chondrules from the Mokoia CV3 carbonaceous chondrite.
740 *Geochimica et Cosmochimica Acta* **68,** 3423–3438.
741 Kadlag Y., Tatzel M., Frick D. A., Becker H. (2019) The origin of unequilibrated EH chondrites –
742 Constraints from in situ analysis of Si isotopes, major and trace elements in silicates and
743 metal, *Geochimica et Cosmochimica Acta* **267**, 300-321
744
745 Keil K. (1968) Mineralogical and chemical relationships among enstatite chondrites. *Journal of*
746 *Geophysical Research* **73,** 6945-6976.
747
748 Kimura M., Hiyagon H., Lin Y. and Weisberg M. K. (2003) FeO-rich silicate components in the
749 Sahara 97159 (EH3) enstatite chondrite: Their mineralogy, oxygen isotopic compositions and
750 origin. *Meteoritics and Planetary Science* **38**, 389-398.
751
752 Kita N. T., Nagahara H., Tachibana S., Tomomura S., Spicuzza M. J., Fournelle J. H. and Valley
753 J. W. (2010) High precision SIMS oxygen three isotope study of chondrules in LL3 chondrites:
754 role of ambient gas during chondrule formation. *Geochimica et Cosmochimica Acta* **74**, 6610–
755 6635.
756
757 Kita N. T., Tenner T. J., Defouilloy C., Nakashima D., Ushikubo T. and Bischoff A. (2015) Oxy-
758 gen isotope systematics of chondrules in R3 clasts: A genetic link to ordinary chondrites. *Lunar*
759 *and Planetary Science Conference* **46**, 2053.
760

761 Kita N. T., Tenner T. J., Ushikubo T., Nakashima D. and Bischoff A. (2013) Primitive chondrules
762 in a highly unequilibrated clast in NWA 753 R chondrite. *Lunar and Planetary Science Con-*
763 *ference* **44**, # 1784 (abstr.)
764
765 Krot A. E., Libourel G., Goodrich C. A. and Petaev M. I. (2004) Silica-rich igneous rims around
766 chondrules in CR carbonaceous chondrites: Evidence for condensation origin from fraction-
767 ated nebular gas. *Meteoritics and Planetary Science* **39**, 1931-1955.
768
769 Krot A. E., Petaev M. I., Russell S. S., Itohc S., Fagan T. J., Yurimoto H., Chizmadia L., Weisberg
770 M. K., Komatsui M., Ulyanovj A. A. and Keil K. (2004) Amoeboid olivine aggregates and
771 related objects in carbonaceous chondrites: records of nebular and asteroid processes. *Chemie*
772 *der Erde* **64**, 185-239.
773
774 Kruijer T. S., Burkhardt, C., Budde, G. and Kleine, T. (2017) Age of Jupiter inferred from the
775 distinct genetics and formation times of meteorites. *Proceeding of the National Academy of*
776 *Science* **114 (26),** 6712-6716.
777
778 Kunihiro T., Rubin A. E., McKeegan K. D. and Wasson J. T. (2004) Oxygen-isotopic compositions
779 of relict and host grains in chondrules in the Yamato 81020 CO3.0 chondrite. *Geochimica et*
780 *Cosmochimica Acta* **68**, 3599–3606.
781
782 Lehner S. W., Buseck P. R. and McDonough W. F. (2010) Origin of kamacite, schreibersite, and
783 perryite in metal-sulfide nodules of the enstatite chondrite Sahara 97072 (EH3). *Meteoritics*
784 *and Planetary Science* **45**, 289–303.

Lehner S. W., McDonough W. F., and P. Nemeth P. (2014) EH3 matrix mineralogy with major and trace element composition compared to chondrules. *Meteoritics and Planetary* Science **49**, 2219–2240.

Lehner S. W., Petaev M. I., Zolotov M. Y. And Buseck P. R. (2013) Formation of niningerite by silicate sulfidation in EH3 enstatite chondrites. *Geochimica et Cosmochimica Acta* **101**,34-56.

Libourel, G., Krot, A. N. and Tissandier L. (2006), Role of gas–melt interaction during chondrule formation, *Earth and Planetary Science Letters* **251**, 232–240.

Libourel G. and Portail (2018) Chondrules as direct thermochemical sensors of solar protoplanetary disk gas. *Science Advances* 4 (7), eaar3321.

Lin Y., Ouyang Z. and El Goresy A. (2002) A. FeO-rich silicates and Ca, Al-rich inclusions in Qingzhen and Yamato 691 (EH3) meteorites: Evidence for migration of mass in the solar nebula. *Chinese Science Bulletin* **47,** 150–153.

Lin, Y., El Goresy, A., Boyet, M., Feng, L., Zhang, J. & Hao, J. (2011), Earliest Solid Condensates Consisting of the Assemblage Oldhamite, Sinoite, Graphite and Excess 36S in Lawrencite from Almahata Sitta MS-17 EL3 Chondrite Fragment. *in 'Workshop on Formation of the First Solids in the Solar System'*, **Vol. 1639** of LPI Contributions, p. 9040.

808 Lin Y., Kimura M., Hiyagon H. and Monoi A. (2003) Unusually abundant refractory inclusions
809 from Sahara 97159 (EH3): a comparative study with other groups of chondrites. *Geochimica*
810 *et Cosmochimica Acta* **67**, 4935-4948.
811
812 Lusby D., Scott E.R.D. and Keil K. (1987) Ubiquitous high FeO silicates in enstatite chondrites.
813 *Proceeding Lunar and Planetary Science Conference 17, Journal of Geophysicl Research.*
814 *Supplement* **92**, E679-E695.
815
816 Marrocchi Y., Euverte R., Villeneuve J., Batanova V., Welsch B., Ferrière L. And Jacquet E.
817 (2019) Formation of CV chondrules by recycling of amoeboid olivine aggregate-like precur-
818 sors. *Geochimica et Cosmochimica Acta* **247**, 121-141.
819
820 Marrocchi Y. And Libourel G. (2013) Sulfur and sulfides in chondrules. *Geochimica et Cosmo-*
821 *chimica Acta,***119**, 2013,117-136.
822
823 Marrocchi Y., Villeneuve J., Batanova V., Piani L. and Jacquet E. (2018) Oxygen isotopic diver-
824 sity of chondrule precursors and the nebular origin of chondrules. *Earth and Planetary Science*
825 *Letters* **496**, 132–141.
826
827 Nagahara H., Kita N. T., Ozawa K. And Morishita Y. (2008) Condensation of major elements
828 during chondrule formation and its implication to the origin of chondrules. *Geochimica et Cos-*
829 *mochimica Acta* **72**,1442-1465.
830
831 Nittler L. R., Starr R. D., Weider S. Z., McCoy T. J., Boynton W, V., Ebel D. S., Ernst C. M.,

Evans L. G., Goldsten J. O., Hamara D. K., Lawrence D. J., McNutt R. L. Jr., Schlemm C. E. II, Solomon S. C. and Sprague A. L. (2011) The major-element composition of Mercury's surface from MESSENGER X-ray spectrometry. *Science* **333**, 1847-1850.

Paniello R., Day J.M.D., and Moynier F. (2012) Zn isotopic evidence for the origin of the Moon. *Nature* **490**, 376-379.

Piani L., Marrocchi Y., Libourel G., and Tissandier L. (2016) Magmatic sulfides in the porphyritic chondrules of EH enstatite chondrites, *Geochimica et Cosmochimica Acta* **195**, 84-99.

Piani L., Marrocchi Y., Rigaudier T., Vacher L. G., Thomassin D., and Marty B. (2020) Earth's water may have been inherited from material similar to enstatite chondrite meteorites. *Science* **369**, 1110-1113

Pouchou J. L. and Pichoir F. (1991) Quantitative analysis of homogeneous or stratified microvolumes applying the model "PAP". *In Electron Probe Quantitation* (eds. K. F. J. Heinrich and D. E. Newbury). Plenum Press, New York, NY, pp. 31–75.

Rambaldi E. R., Rajan R. S., Wang D. and Housley R. M. 1983. Evidence for RELICT grains in chondrules of Qingzhen, an E3 type enstatite chondrite. *Earth and Planetary Science Letters* **66**, 11–24.

Rubin A. E. (1983) The Adhi Kot breccia and implications for the origin of chondrules and silica-rich clasts in enstatite chondrites. *Earth and Planetary Science Letters* **64**, 201-212.

Rudraswami N. G., Ushikubo T., Nakashima D. and Kita N. T. (2011) Oxygen isotope systematics of chondrules in Allende CV3 chondrite: high precision ion microprobe studies. *Geochimica et Cosmochimica. Acta* **75**, 7596–7611.

Sakamoto N., Seto Y., Itoh S., Kuramoto K., Fujino K., Nagashima K., Krot A. N. and Yurimoto H. (2007) Remnants of the early solar system water enriched in heavy oxygen isotopes. *Science* **317**, 231–233.

Savage P. S. and Moynier F. (2013) Silicon isotopic variation in enstatite meteorites: Clues to their origin and Earth-forming material. *Earth and Planetary Science Letters* **361**, 487–496.

Schneider J. M., Burkhardt C., Marrocchi Y., Brennecka G. A., and Kleine T. (2020) Early evolution of the solar accretion disk inferred from Cr-Ti-O isotopes in individual chondrules, *Earth and Planetary Science Letters* **551**, 116585.

Schrader D. L., Connolly H. C. Jr., Lauretta D. S., Nagashima K., Huss G. R., Davidson J., and Domanik K. J. (2013) The formation and alteration of the Renazzo-like carbonaceous chondrites II: Linking O-isotope composition and oxidation state of chondrule olivine. Geochimica et Cosmochimica Acta **101**, 302-327.

Schrader D. L., Nagashima K., Davidson J., McCoy T. jJ., Ogliore R. C., and Fu R. R. (2020) Outward migration of chondrule fragments in the early Solar System: O-isotopic evidence for rocky material crossing the Jupiter Gap? *Geochimica et Cosmochimica Acta* **282**,133-155.

880 Schrader D. L., Nagashima K., Krot A. N., Ogliore R. C., and Hellebrand E. (2014) Variations in
881 the O-isotope composition of gas during the formation of chondrules from the CR chondrites.
882 Geochimica et Cosmochimica Acta **132**, 50-74.
883
884 Schrader D. L., Nagashima K., Krot A. N., Ogliore R. C., Yin Q.-Z., Amelin Y., Stirling C. H.,
885 and Kaltenbach A. (2017) Distribution of ^{26}Al in the CR chondrite chondrule-forming region
886 of the protoplanetary disk. Geochimica et Cosmochimica Acta **201**, 275-302.
887
888 Sikdar J. and Rai V. K. (2020) Si-Mg isotopes in enstatite chondrites and accretion of reduced
889 planetary bodies. *Scientific Report* **10,** 1273.
890
891 Simon S. B., Sutton S. R. and Grossman L. (2016) The valence and coordination of titanium in
892 ordinary and enstatite chondrites. *Geochimica et Cosmochimica Acta* **189**, 377–390.
893
894 Tanaka R. and Nakamura E. (2017) Silicate-SiO reaction in a protoplanetary disk recorded by
895 oxygen isotopes in chondrules. *Nature Astronomy* **1**, 0137.
896
897 Tenner T. J., Nakashima D., Ushikubo T., Kita N. T. and Weisberg M.K. (2015) Oxygen isotope
898 ratios of FeO-poor chondrules in CR3 chondrites: Influence of dust enrichment and H_2O during
899 chondrule formation. *Geochimica et Cosmochimica Acta* **148**, 228-250.
900
901 Tenner T. J., Kimura M. and Kita N. T. (2017). Oxygen isotope characteristics of chondrules from
902 the Yamato-82094 ungrouped carbonaceous chondrite: Further evidence for common O-
903 isotope environments sampled among carbonaceous chondrites. *Meteoritics and Planetary*

Science **52**, 268-294.

Tissandier, L., Libourel G., and Robert F. (2002), Gas-melt interactions and their bearing on chondrule formation. *Meteoritics and Planetary Science* **37**, 1377–1389.

Trinquier A., Elliott T., Ulfbeck D., Coath C., Krot A. N. and Bizzarro M. (2009) Origin of nucleosynthetic isotope heterogeneity in the Solar protoplanetary disk. *Science* **324**, 374-376.

Ushikubo T., Kimura M., Kita N. T. and Valley J. W. (2012) Primordial oxygen isotope reservoirs of the solar nebula recorded in chondrules. *Geochimica et Cosmochimica Acta* **90**, 242-264.

Van Niekerk D. and Keil K. (2011) Metal/sulfide silicate intergrowth textures in EL3 mreteorites: Origin by impact melting on the EL parent body. *Meteoritics and Planetary Sciences* **46**, 1484–1497

Warren P. H. (2011) Stable-isotopic anomalies and the accretionary assemblage of the Earth and Mars: A subordinate role for carbonaceous chondrites. *Earth and Planetary Science Letters* **311**, 93–100.

Weisberg M. K., Ebel D. S. and Connolly H. C. Jr. (2013) EL3 chondrites: Primitive nebular materials, not products of asteroidal Processing. **44th** *Lunar and Planetary Science Conference*, abstract # 2871.

927 Weisberg M. K., Ebel D. S., Connolly H. C. Jr., Kita N. T. and Ushikubo T. (2011) Petrology and
928 oxygen isotope compositions of chondrules in E3 chondrites. *Geochimica et Cosmochimica*
929 *Acta* **75**, 6556-6569.
930
931 Weisberg M. K., Ebel D. S. and Kimura M. (2012b) Petrology of chondrules and a diopside-rich
932 inclusion in the MAC 88136 EL3 chondrite. *75th Annual Meeting of the Meteoritical Society*,
933 abstract #5228
934
935 Weisberg M. K. and Kimura M. (2012) The unequilibrated enstatite chondrites. *Chemie der Erde*
936 **72**, 101-115.
937
938 Weisberg M. K., Prinz M., and Fogel R.A. (1994) The evolution of enstatite and chondrules in
939 unequilibrated enstatite chondrites: Evidence from iron-rich pyroxene. *Meteoritics* **29**, 362-
940 373.
941
942 Weisberg M. K., Ebel D. S., Kimura M., Kita N. T., and Nakashima D. (2010) Petrology and
943 oxygen isotopes of chondrules in the Kota-Kota EH3 Chondrite. *41st Lunar and Planetary*
944 *Science Conference*, abstract #1756.
945
946 Weisberg M. K., Zolensky M. E., Howard K. T., Kimura M., Ebel D. S., Alexander C. M. O'D.
947 and Boleaga Y. (2020) Petrologic evidence of hydrothermal activity on the EL3 parent aster-
948 oid. *Lunar and Planetary Science Conference* **51**, #1683.
949

Weyrauch M., Horstmann M. and Bischoff A. (2018) Chemical variations of sulfides and metal in enstatite chondrites—Introduction of a new classification scheme. *Meteoritics and Planetary Science* **53**, 394-415.

Williams C. D., Sanborn M. E., Defouilloy C., Yin Q-Z., Kita. N. T., Ebel D. S., Yamakawa A. and Yamashita K. (2020) Chondrules reveal large-scale outward transport of inner Solar System materials in the protoplanetary disk. Online 9/8/2020, *Proc. National Academy Sciences* DOI: 10.1073/pnas.2005235117

Young E.D. and Russell S. S. (1998) Oxygen reservoirs in the early solar nebula inferred from an Allende CAI. *Science* **282**, 452-455.

Yu Y., Hewins R. H., Clayton R. N. and Mayeda T. K. (1995) Experimental-study of high temperature oxygen-isotope exchange during chondrule formation. *Geochimica et Cosmochimica Acta* **59**, 2095–2104.

968 Table 1. Oxygen isotope ratios (‰) and errors and average Mg#s for the chondrules studied from
969 ALH 81189, ALH 85159 EH3 and MAC 88136 EL3 chondrites.
970
971 Figure Captions
972 Figure 1. Mg-Ca-Al (red-green-blue) element maps of the three equilibrated enstatite chondrites
973 studied:. (a) ALH81189, 3 (b) ALH 85169, 5 and (c) MAC 88136, 37. The circled/numbered areas
974 are the chondrules and other inclusions that were studied. The ones circled in white were analyzed
975 for oxygen isotopes. On these maps the brightest reds are forsterite. The duller reds are enstatite
976 which are the dominant silicate. Metal-sulfide-rich nodules appear mostly black. In (c) the green
977 area marked C1 is the diopside-rich portion of the large chondrule CI in MAC 88136.
978
979 Figure 2. Backscattered electron (BSE) images of representative chondrules and fragments in ALH
980 81189 that were analyzed for oxygen isotopes. (a) Olivine mineral fragment that is over 300 μm
981 across. (b) Enstatite-rich chondrule containing minor forsterite, troilite and interstitial Na-Al-
982 bearing mesostasis. This can be classified as a type IB porphyritic pyroxene chondrule and is
983 representative of the chondrules that are common in E3 chondrites. (c) C9 is an irregular shaped
984 object, possibly a broken chondrule, dominated by FeO-bearing pyroxene and minor silica. Such
985 objects are rare in E3 chondrites. (d) C13 is a barred chondrule with larger grains (up to ~40 μm)
986 of enstatite.
987
988 Figure 3. Images of the more unusual objects identified in the E3 chondrites studied. (a) BSE image
989 of a diopside-plagioclase inclusion in ALH 81189. (b) Mg-Ca-Al (red-green-blue) composite
990 element map of an amoeboid olivine aggregate in ALH 81189 consisting of fine olivine
991 surrounding inclusions (refractory nodules) composed of diopside and anorthite. (c) Mg-Ca-Al
992 (red-green-blue) composite element map of CI in MAC 88136, a large (~ 1mm) chondrule
993 composed of diopside and enstatite with silica and Na-Al-rich plagioclase. (d) Si-Ca-Fe (red-
994 green-blue) composite element map of C1 showing that the silica occurs mainly around the edge
995 of the diopside.
996
997 Figure 4. Images of representative metal-rich nodules that were studied. (a) Fe-Ni-S (red-green-

998 blue) composite element map of a nodule in MAC 88136 composed of schriebersite, graphite,
999 troilite, daubreelite and enstatite surrounded by Si-bearing FeNi metal alloy (red). (b) BSE image
1000 of a metal-rich nodule in ALH 81189 composed of Si-bearing FeNi metal (white), troilite (medium
1001 grey) and enstatite (dark grey). (c) BSE of a metal-rich nodule composed of Is-bearing FeNi metal
1002 intergrown with laths of enstatite. (d) BSE of a cluster of metal-rich nodules in MAC 88136
1003 composed of Si-bearing FeNi (bright white), numerous enstatite laths (dark grey) and graphite
1004 (black). Oxygen isotopes were analyzed in all these metal nodules.
1005
1006 Figure 5. Histograms showing the silicate compositions in the chondrules and other objects in the
1007 three E3 chondrites that were studied. As expected, all three E3 chondrites are dominated by
1008 enstatite with near end-member composition. Most olivine is also near end-member forsterite.
1009 FeO-bearing silicates are much less common.
1010
1011 Fig. 6 Oxygen three-isotope ratios of chondrules in E3 chondrites. (a) Oxygen isotopic ratios of
1012 individual spot analyses. Data plot along primitive chondrule mineral (PCM) line (Ushikubo et al.,
1013 2012), but mostly clustering at its intersection with the terrestrial fractionation line (TF). Other
1014 lines are from Young and Russell (1998, Y-R), and the carbonaceous chondrite anhydrous mineral
1015 line (CCAM, Clayton and Mayeda, 1984). (b) Oxygen 3-isotope diagram showing average oxygen
1016 isotope ratios for each chondrule analyzed in ALH 81189, ALH 85159 and MAC 88136. A blue
1017 dashed line is drawn parallel to the PCM line through seven E chondrite objects that lie above the
1018 PCM, possibly forming a second trend. (c) Oxygen isotope ratios of an AOA in ALH 81189, relict
1019 olivine in ALH 81189 C1, and individual pyroxene analyses from ALH 85159 C51. Inset enlarges
1020 the data from ALH 85159 C51 and ALH 81189 C1 which plot above the TF line. (d) E3 chondrules
1021 are plotted in two groups; majority of chondrules that plot on the PCM line and *other chondrules*
1022 that along with relict olivine in ALH 81189 C1 and heterogeneous chondrule ALH 85159 C51.
1023 The regression lines (dashed lines) and MSWD of the fits of two groups are shown. Chondrule
1024 data from LL3 chondrites are shown as comparison. (e) Data from our previous work on other E3
1025 chondrites (Weisberg et al., 2011) showing a similar trend with some chondrule olivine plotting
1026 toward more ^{16}O-rich compositions. E3 chondrules determined from bulk methods (C&M1985:

Clayton and Mayeda, 1985; T&N2017: Tanaka and Nakamura, 2017) are also show, which generally agree within the range observed in our new dataset. (f) The regression line of all E3 chondrule data. Data used for estimating regression lines is shown in EA4.

Fig 7. (a) Average $\Delta^{17}O$ vs. average Mg# for the type I (FeO-poor) chondrules, fragments and metal-rich nodules in ALH 81189 EH3, paired ALH 85159 and MAC 88136 EL3 chondrites. (b) Average $\Delta^{17}O$ vs. average Mg# for all chondrules from this study and Weisberg et al. (2011). The lines are best fit lines through the data (r=0.2). The AOA is not included.

Fig. 8. Comparison of the chondrule oxygen isotope data for E chondrite chondrules to those in Acfer 094 and CR, CV and CM carbonaceous chondrites and LL ordinary chondrites. Data from this study, Ushikubo et al. (2012), Chaumard et al. (2018), Tenner et al. (2015)' Hertwig et al. (2018, 2019b), Kita et al. (2010).

Captions for Supplementary Materials

Figure S1. BSE images (left) and SE images (right) of the chondrules from ALH 81189,3, ALH 85159, 5 and MAC 88136, 37 that were analyzed in this study. Images on the right show SIMS spots and images on the left show the pits from the analyses.

Table S1. Mineral compositions (wt. % oxide) of the chondrules studied.

Table S2. Oxygen isotopic compositions of the standards measured using SIMS for calibration of instrumental mass fractionation.

Table S3. Oxygen isotopic compositions of the minerals analyzed in the chondrules from ALH 81189, 3, ALH 85159, 5 and MAC 88136, 37.

Table S4. Data from this study and Weisberg et al. (2011) used for estimating the regression in Fig. 6f.

1057

Table 1. Oxygen isotope ratios (‰) and errors and average Mg#s for the chondrules studied from ALH 81189, ALH 85159 EH3 and MAC 88136 EL3 chondrites.

Meteorite	sample	Type	Phase	Avg. Mg#	N for mean*	δ18O (‰)	Unc.	δ17O (‰)	Unc.	Δ17O (‰)	Unc.
ALH 81189	C1	PP	En	99.3	5	6.08	0.46	3.96	0.28	0.80	0.13
ALH 81189	C5	PP	En	98.4	6	5.10	0.33	2.44	0.18	-0.21	0.12
ALH 81189	C9	PP	Pyx	81.0	6	4.34	0.34	1.76	0.23	-0.49	0.17
ALH 81189	C10	PO	Fo, En	98.3	6	5.08	0.32	2.38	0.18	-0.26	0.14
ALH 81189	C11	PP	Ol, En	98.7	6	5.17	0.35	3.53	0.31	0.85	0.22
ALH 81189	C13	Barred	Fo, En	99.0	6	4.41	0.35	1.64	0.27	-0.65	0.16
ALH 81189	C14	PP	En	98.9	6	5.23	0.32	2.45	0.25	-0.27	0.17
ALH 81189	C15	PP	En	98.8	6	5.34	0.32	2.72	0.26	-0.05	0.20
ALH 81189	C21	POP	Fo, En	98.8	4	4.73	0.39	2.35	0.27	-0.11	0.16
ALH 81189	C22	PP	En	99.3	4	2.33	0.50	-0.15	0.23	-1.36	0.16
ALH 81189	C23	PP	En	98.2	6	5.08	0.38	2.70	0.24	0.05	0.22
ALH 81189	C27	PP	En	99.1	1	6.40	0.40	4.13	0.28	0.81	0.21
ALH 81189	C30	PP	En	98.8	6	4.83	0.34	2.31	0.30	-0.20	0.20
ALH 81189	C31	POP	En	99.1	6	5.48	0.31	3.84	0.21	0.99	0.13
ALH 81189	C33	PP	En	98.1	6	5.30	0.36	2.78	0.23	0.03	0.16
ALH 81189	C38	PP	En	99.3	6	4.73	0.43	2.26	0.23	-0.20	0.14
ALH 81189	F1	Min Frag	Ol	98.0	4	4.86	0.32	2.35	0.22	-0.17	0.16
ALH 81189	F2	Min Frag	Ol	98.3	4	4.91	0.34	2.36	0.19	-0.19	0.18
ALH 81189	F5	PO	En	98.7	6	4.42	0.34	1.99	0.19	-0.31	0.12
ALH 81189	F9	Diops-plag	En	97.7	3	4.06	0.85	1.47	0.61	-0.64	0.19
ALH 81189	F17	AOA	Ol	99.7	2	-46.49	0.34	-47.98	0.24	-23.81	0.20
ALH 81189	M5	MN	En	98.5	4	4.44	0.43	2.09	0.30	-0.22	0.18
ALH 85159	C7	PP	En	99.1	6	5.77	0.65	3.25	0.35	0.25	0.12
ALH 85159	C13	PP	En	99.2	6	5.54	0.35	2.70	0.25	-0.18	0.18
ALH 85159	C25	PP	En	99.6	5	6.26	0.36	3.55	0.21	0.30	0.15
ALH 85159	C43	PP	En	99.8	6	5.97	0.35	3.18	0.20	0.08	0.16
ALH 85159	C46	PP	En	98.5	6	6.39	0.39	3.54	0.32	0.22	0.19
ALH 85159	C47	PP	En	99.4	6	6.57	0.40	3.76	0.19	0.34	0.13
ALH 85159	C50	PP	En	99.1	6	6.28	0.39	3.44	0.26	0.17	0.12
ALH 85159	C51	PP	En	99.3	6	6.85	0.78	4.84	0.61	1.27	0.24
ALH 85159	C52	PP	En	98.9	6	5.82	0.37	2.79	0.23	-0.24	0.18
MAC 88136	C1	Diops-rich	Diops/En	99.4	4	5.15	0.32	2.64	0.21	-0.04	0.16
MAC 88136	C1	Diops-rich	silica		1	8.33	0.15	4.22	0.23	-0.12	0.25
MAC 88136	C1	Diops-rich	Silica		1	8.42	0.15	4.26	0.23	-0.12	0.25
MAC 88136	C3	PP	En	99.6	6	5.40	0.40	2.69	0.33	-0.12	0.19
MAC 88136	C6	PP	En	99.6	6	5.51	0.40	2.51	0.31	-0.35	0.20
MAC 88136	C7	PP	En	99.5	5	5.31	0.32	2.39	0.25	-0.38	0.21
MAC 88136	C9	PP	En	99.5	6	6.42	0.34	4.34	0.35	1.00	0.28
MAC 88136	C10	PP	En	99.6	6	5.45	0.35	2.94	0.38	0.11	0.30
MAC 88136	C11	BP	En	99.5	7	5.95	0.34	3.17	0.32	0.07	0.29
MAC 88136	C16	PP	En	99.0-99.9	6	5.93	0.34	3.10	0.25	0.01	0.20
MAC 88136	C17	PP	En	99.4	6	5.65	0.32	2.94	0.28	0.00	0.27
MAC 88136	C30	Silica-rich	Silica		1	8.73	0.15	4.55	0.23	0.01	0.25
MAC 88136	M1	MN	En	NA	4	5.55	0.35	2.81	0.24	-0.08	0.17
MAC 88136	M8	MN	En	98.8	2	5.81	0.38	3.07	0.27	0.05	0.19
MAC 88136	M10	MN	En	99.3	3	5.74	0.45	3.02	0.40	0.04	0.27

Unc. - Uncertainties of host oxygen isotope ratios are propagated, combining the 2SE of chondrule measurements.
Mg# = Mg/(Mg+Fe) X 100 and is the average value for pyroxene and/or olivine for each chondrule.
Phases: En-enstatite, Ol- olivine, Pyx - pyroxene, diops-diopside
Chondrule types: PP- porphyritic pyroxene, POP- porphyritic olivine and pyroxene, PO - porphyritic olivine, Min Frag - mineral fragment, AOA - amoeboid olivine aggregate, MN - metal-rich nodule.
N - the number analyses averaged for the oxygen isotope compositions given.

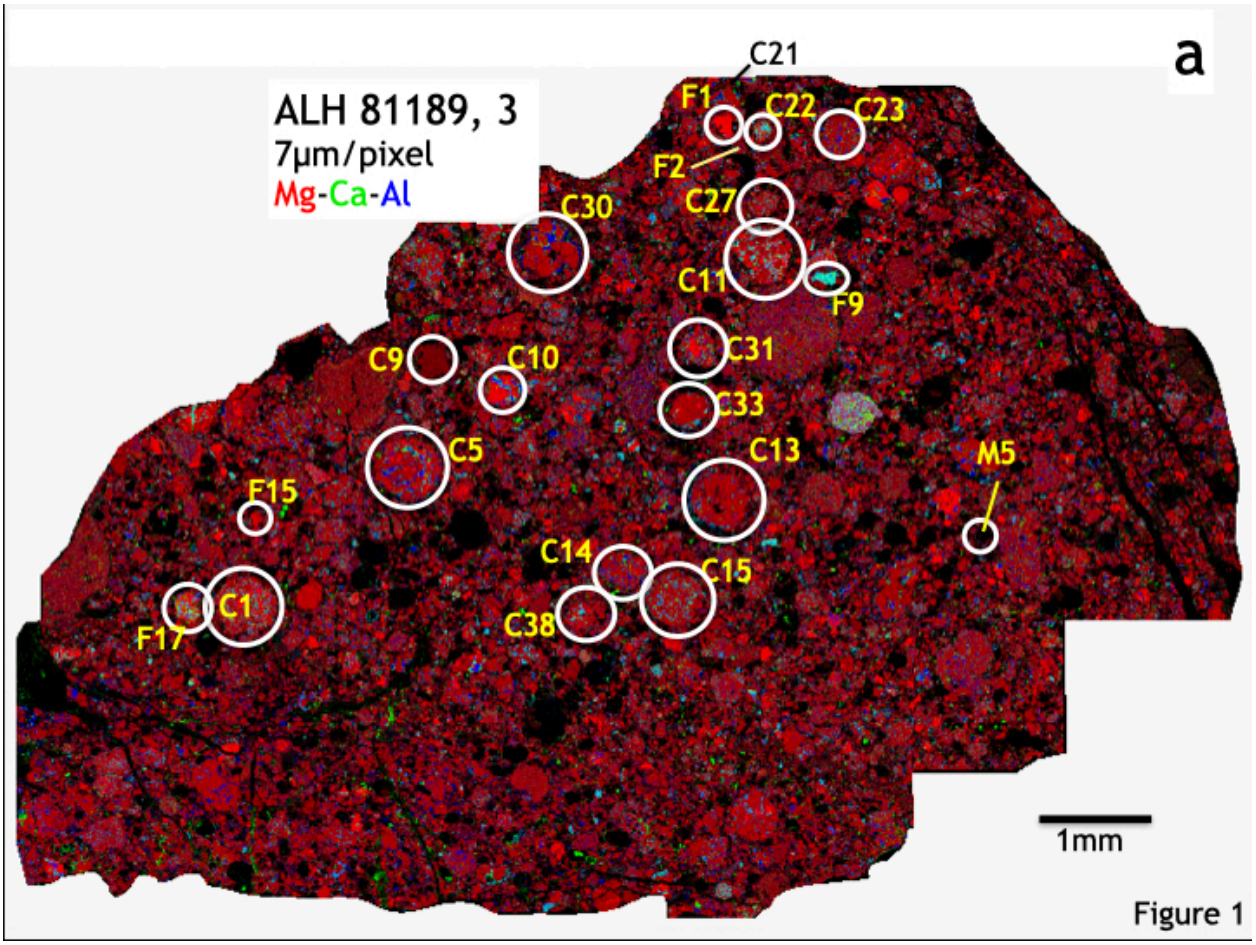

Figure 1

b

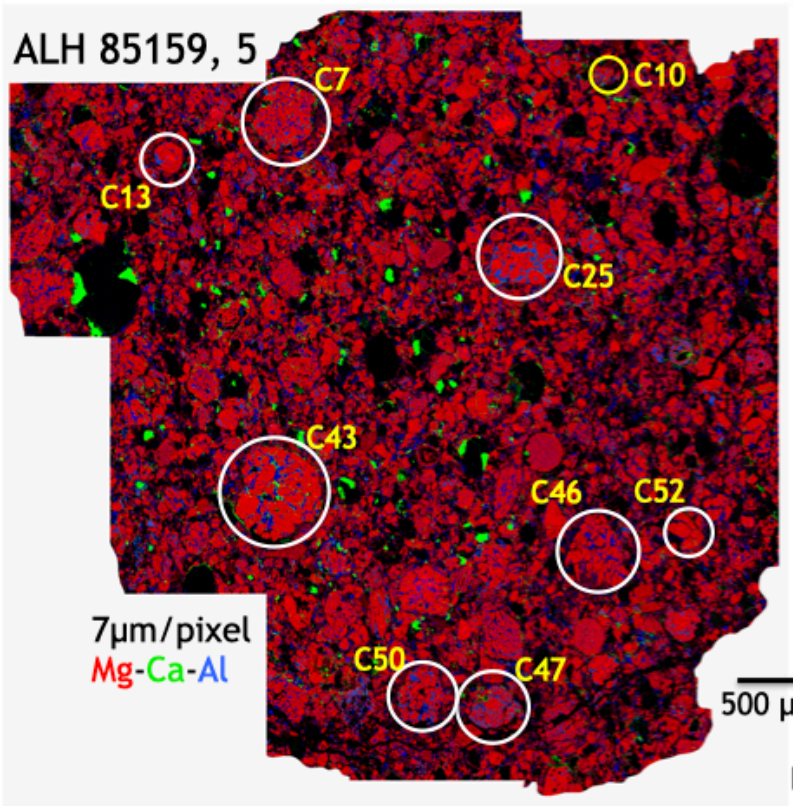

Figure 1

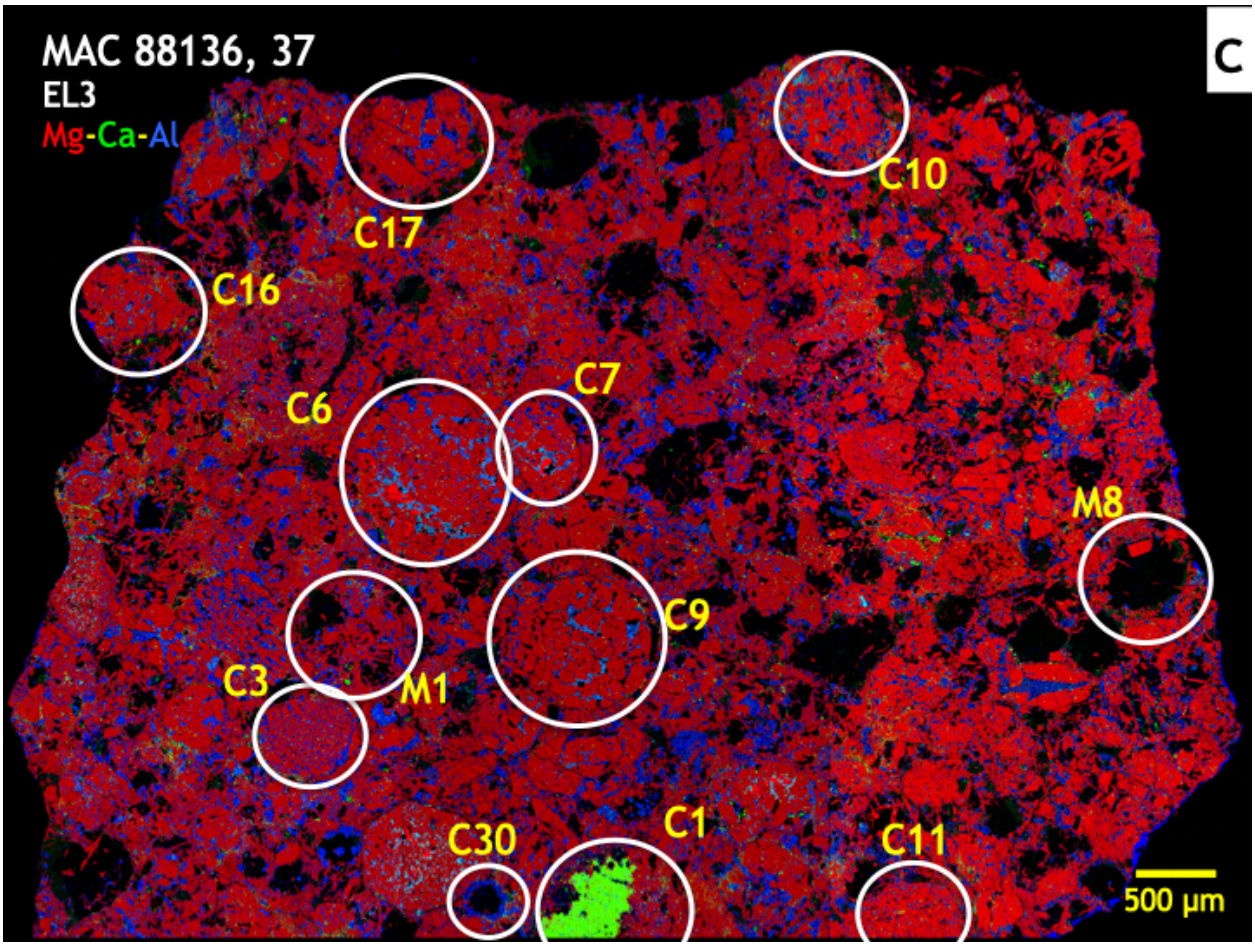
MAC 88136, 37
EL3
Mg-Ca-Al
C
C10
C17
C16
C7
C6
M8
C9
C3
M1
C30
C1
C11
500 µm

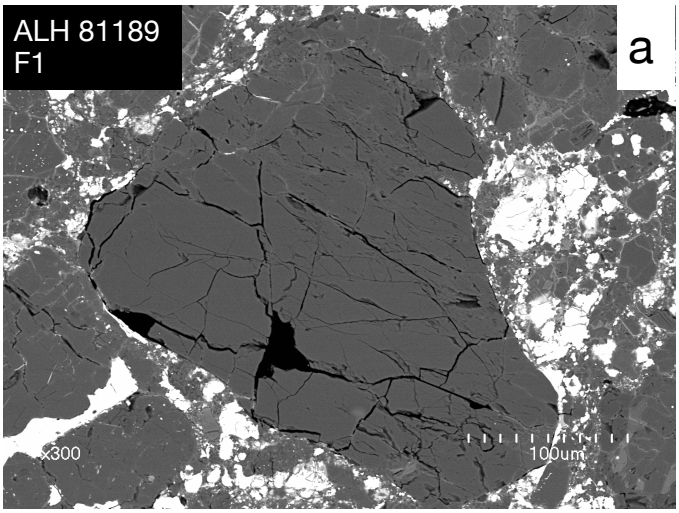
ALH 81189
F1
a
x300
100um

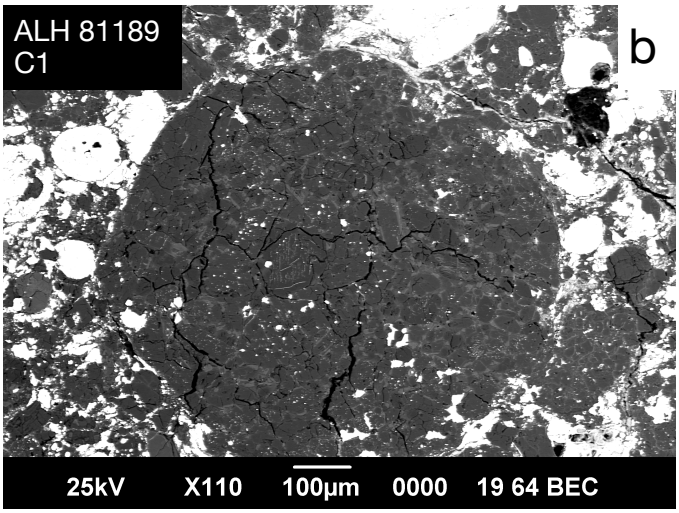
ALH 81189
C1
b
25kV X110 100µm 0000 19 64 BEC

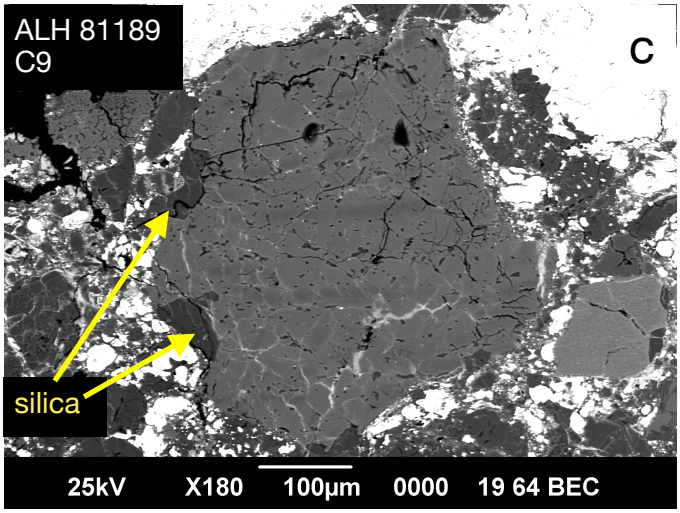
ALH 81189
C9
c
silica
25kV X180 100µm 0000 19 64 BEC

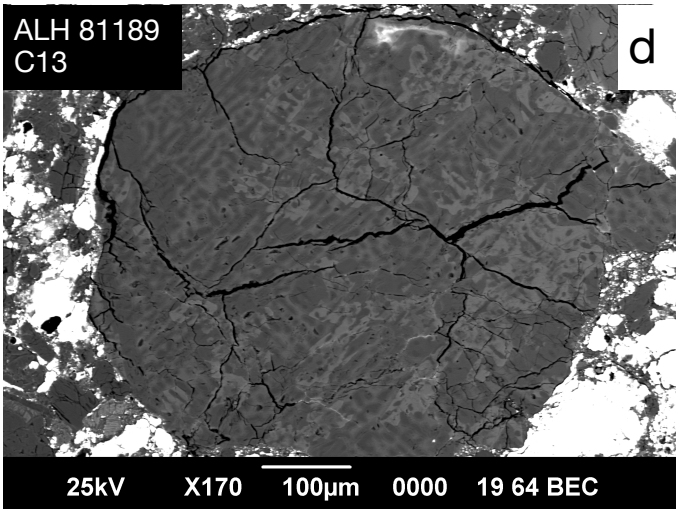
ALH 81189
C13
d
25kV X170 100µm 0000 19 64 BEC

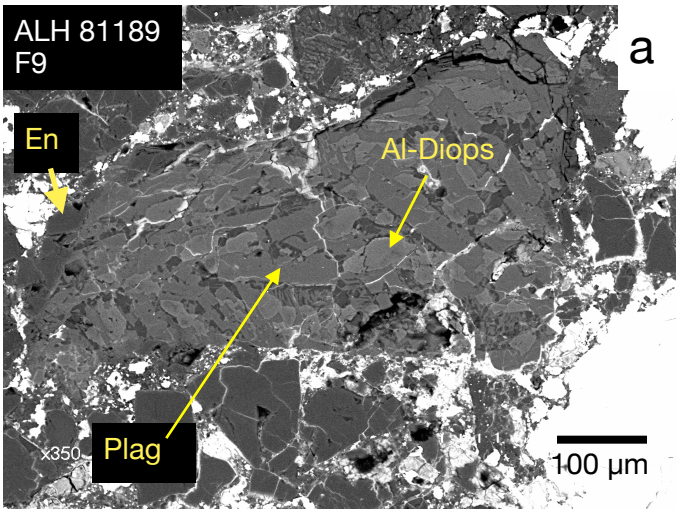
ALH 81189
F9
a
En
Al-Diops
Plag
x350
100 µm

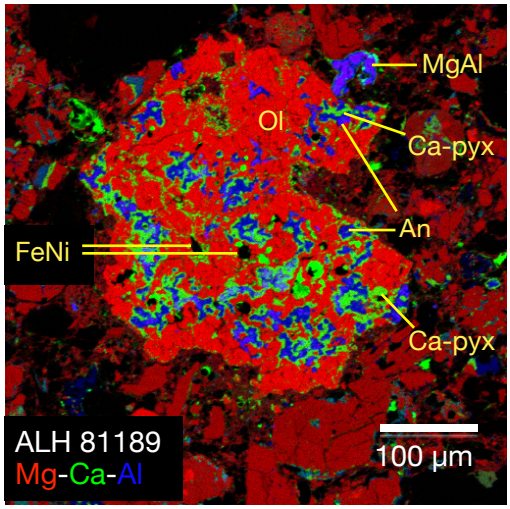
b
MgAl
Ol
Ca-pyx
An
FeNi
Ca-pyx
ALH 81189
Mg-Ca-Al
100 µm

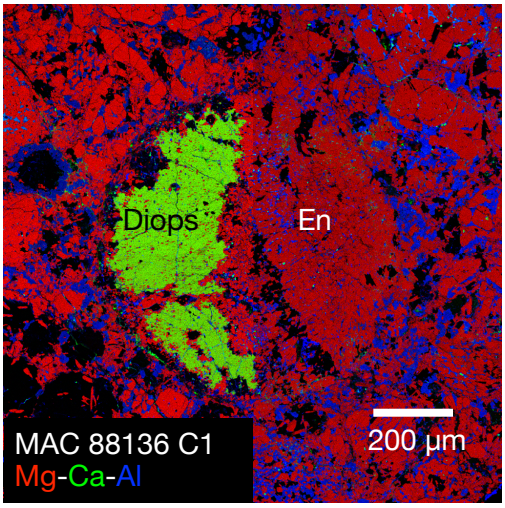
c
Diops
En
MAC 88136 C1
Mg-Ca-Al
200 µm

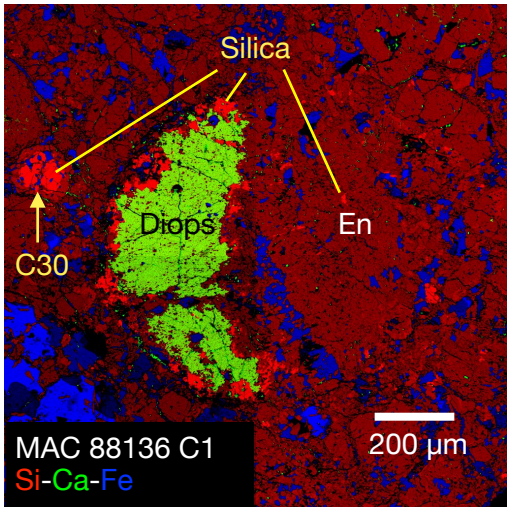
d
Silica
C30
Diops
En
MAC 88136 C1
Si-Ca-Fe
200 µm

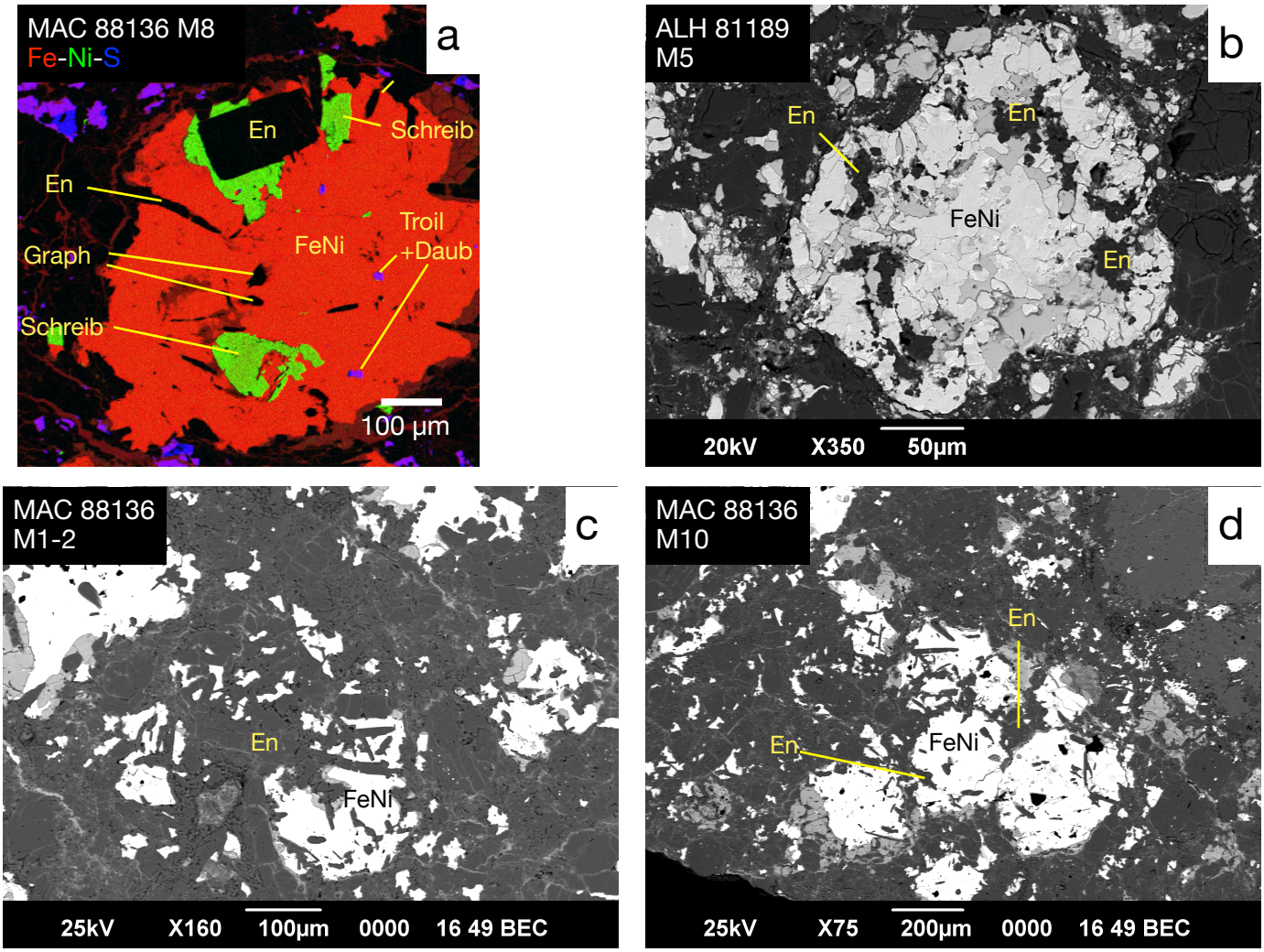
MAC 88136 M8
Fe-Ni-S
a
En
Schreib
En
Troil
+Daub
FeNi
Graph
Schreib
100 µm
ALH 81189
M5
b
En
En
FeNi
En
20kV X350 50µm
MAC 88136
M1-2
c
En
FeNi
25kV X160 100µm 0000 16 49 BEC
MAC 88136
M10
d
En
En
FeNi
25kV X75 200µm 0000 16 49 BEC

Average Silicate Compositions

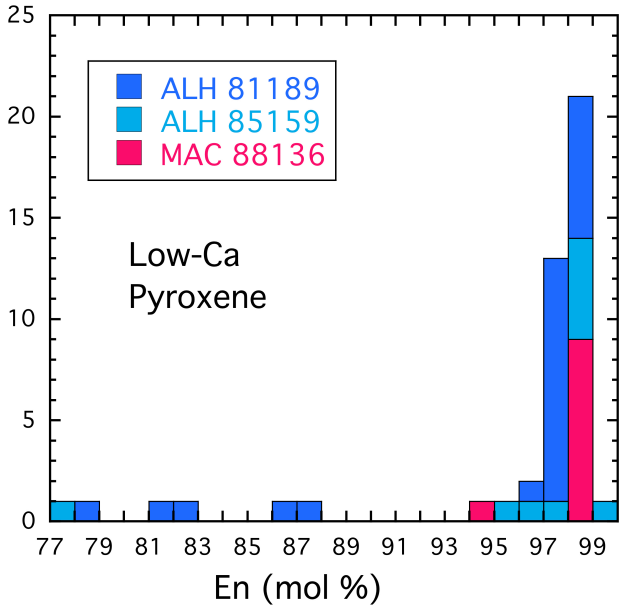

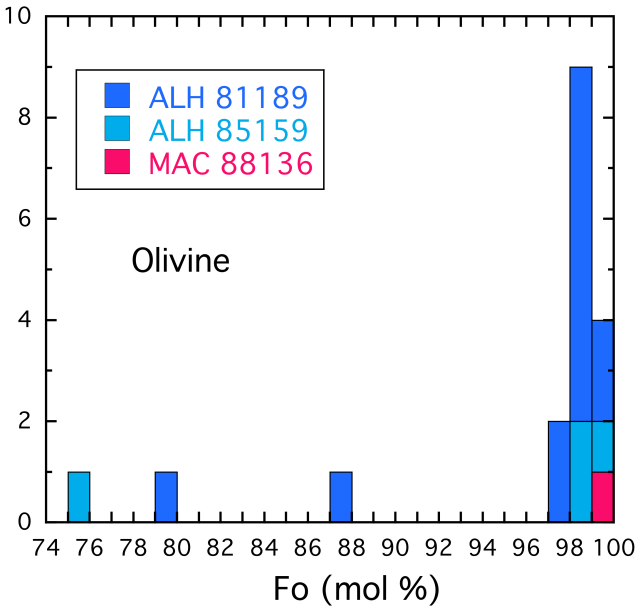

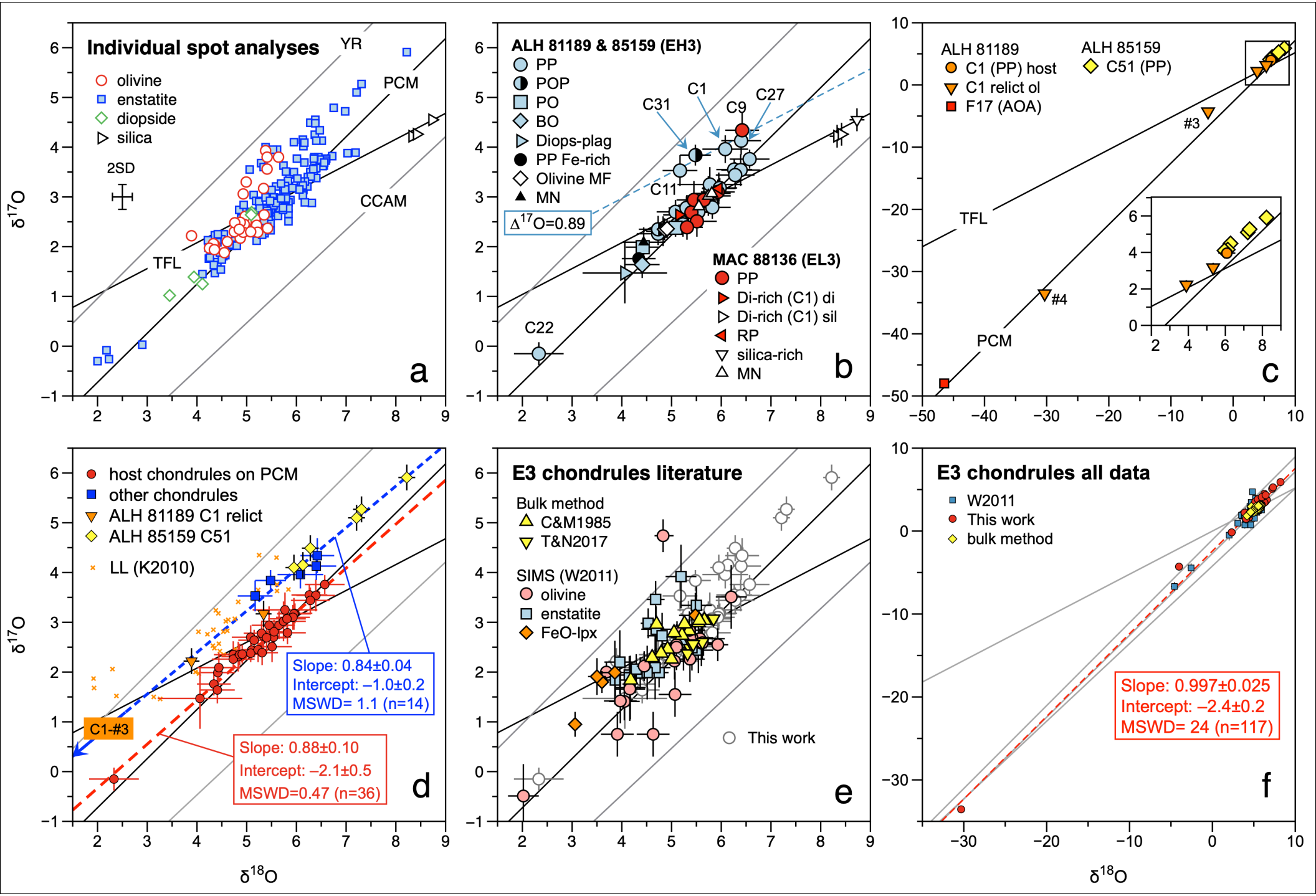
Individual spot analyses
olivine
enstatite
diopside
silica
2SD
YR
PCM
CCAM
TFL
a
ALH 81189 & 85159 (EH3)
PP
POP
PO
BO
Diops-plag
PP Fe-rich
Olivine MF
MN
Δ17O=0.89
C1
C31
C9
C27
C11
C22
MAC 88136 (EL3)
PP
Di-rich (C1) di
Di-rich (C1) sil
RP
silica-rich
MN
b
ALH 81189
C1 (PP) host
C1 relict ol
F17 (AOA)
ALH 85159
C51 (PP)
#3
#4
TFL
PCM
c
host chondrules on PCM
other chondrules
ALH 81189 C1 relict
ALH 85159 C51
LL (K2010)
Slope: 0.84±0.04
Intercept: −1.0±0.2
MSWD= 1.1 (n=14)
C1-#3
Slope: 0.88±0.10
Intercept: −2.1±0.5
MSWD=0.47 (n=36)
d
E3 chondrules literature
Bulk method
C&M1985
T&N2017
SIMS (W2011)
olivine
enstatite
FeO-lpx
This work
e
E3 chondrules all data
W2011
This work
bulk method
Slope: 0.997±0.025
Intercept: −2.4±0.2
MSWD= 24 (n=117)
f
δ17O
δ18O

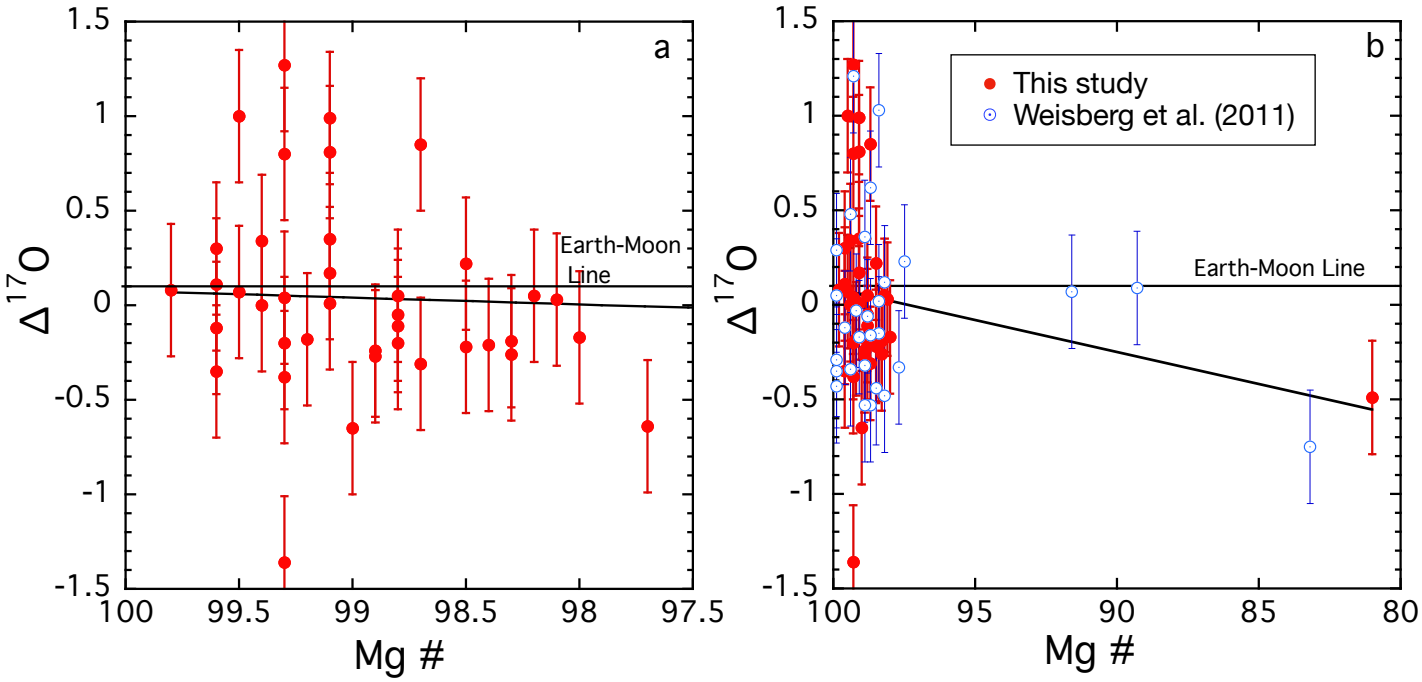
a
b
This study
Weisberg et al. (2011)
Earth-Moon Line
Earth-Moon Line
$\Delta^{17}O$
$\Delta^{17}O$
Mg #
Mg #
1.5
1
0.5
0
-0.5
-1
-1.5
100
99.5
99
98.5
98
97.5
95
90
85
80

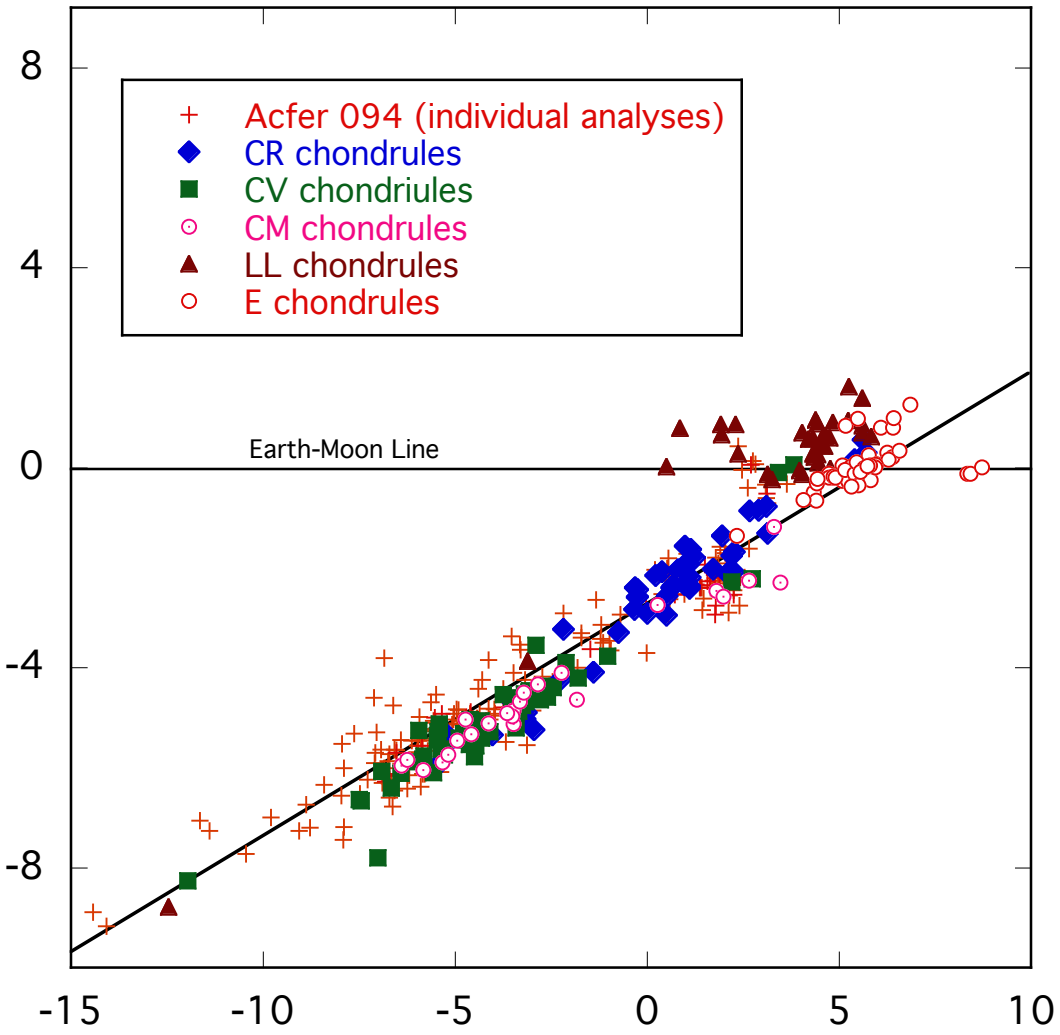
Acfer 094 (individual analyses)
CR chondrules
CV chondriules
CM chondrules
LL chondrules
E chondrules
Earth-Moon Line
8
4
0
-4
-8
-15
-10
-5
0
5
10